

Electronic Thesis and Dissertation Repository

---

5-17-2012 12:00 AM

## Real-time Prostate Motion Tracking For Robot-assisted Laparoscopic Radical Prostatectomy

Mehdi Esteghamatian  
*The University of Western Ontario*

Supervisor  
Terry Peters  
*The University of Western Ontario*

Graduate Program in Biomedical Engineering  
A thesis submitted in partial fulfillment of the requirements for the degree in Master of  
Engineering Science  
© Mehdi Esteghamatian 2012

Follow this and additional works at: <https://ir.lib.uwo.ca/etd>



Part of the [Bioimaging and Biomedical Optics Commons](#), [Biomedical Devices and Instrumentation Commons](#), and the [Vision Science Commons](#)

---

### Recommended Citation

Esteghamatian, Mehdi, "Real-time Prostate Motion Tracking For Robot-assisted Laparoscopic Radical Prostatectomy" (2012). *Electronic Thesis and Dissertation Repository*. 549.  
<https://ir.lib.uwo.ca/etd/549>

This Dissertation/Thesis is brought to you for free and open access by Scholarship@Western. It has been accepted for inclusion in Electronic Thesis and Dissertation Repository by an authorized administrator of Scholarship@Western. For more information, please contact [wlsadmin@uwo.ca](mailto:wlsadmin@uwo.ca).

REAL-TIME PROSTATE MOTION TRACKING FOR ROBOT-ASSISTED  
LAPAROSCOPIC RADICAL PROSTATECTOMY

(Spine title: Real-time Prostate Motion Tracking for RARP)

(Thesis format: Integrated Article)

by

Mehdi Esteghamatian

Graduate Program in Biomedical Engineering

A thesis submitted in partial fulfillment  
of the requirements for the degree of  
Master of Engineering Science

The School of Graduate and Postdoctoral Studies  
Western University  
London, Ontario, Canada

© Mehdi Esteghamatian 2012

WESTERN UNIVERSITY  
School of Graduate and Postdoctoral Studies

**CERTIFICATE OF EXAMINATION**

Supervisor:

.....  
Dr. T. M. Peters

Supervisory Committee:

.....  
Dr. S. E. Pautler

.....  
Dr. H. Ladak

.....  
Dr. C. McKenzie

Examiners:

.....  
Dr. A. Fenster

.....  
Dr. A. Ward

.....  
Dr. S. deRibaupierre

The thesis by

**Mehdi Esteghamatian**

entitled:

**Real-time Prostate Motion Tracking for Robot-Assisted Laparoscopic Radical  
Prostatectomy**

is accepted in partial fulfillment of the  
requirements for the degree of  
Master of Engineering Science

.....  
Date

.....  
Chair of the Thesis Examination Board

## Abstract

Radical prostatectomy surgery (RP) is the gold standard for treatment of localized prostate cancer (PCa). Recently, emergence of minimally invasive techniques such as Laparoscopic Radical Prostatectomy (LRP) and Robot-Assisted Laparoscopic Radical Prostatectomy (RARP) has improved the outcomes for prostatectomy. However, it remains difficult for surgeons to make informed decisions regarding resection margins and nerve sparing since the location of the tumour within the organ is not usually visible in a laparoscopic view. While MRI enables visualization of salient structures and cancer foci, its efficacy in LRP is reduced unless it is fused into a stereoscopic view such that homologous structures overlap. Registration of the MR image and peri-operative ultrasound image either via visual manual alignment or using a fully automated registration can potentially be exploited to bring the pre-operative information into alignment with the patient coordinate system at the beginning of the procedure. While doing so, prostate motion needs to be compensated in real-time to synchronize the stereoscopic view with the pre-operative MRI during the prostatectomy procedure. In this thesis, two tracking methods are proposed to assess prostate rigid rotation and translation for prostatectomy. The first method presents a 2D-to-3D point-to-line registration algorithm to measure prostate motion and translation with respect to an initial 3D TRUS image. The second method investigates a point-based stereoscopic tracking technique to compensate for rigid prostate motion so that the same motion can be applied to the pre-operative images.

**Keywords:** Robotic-assisted Laparoscopic Radical Prostatectomy, Laparoscopic Surgery, Motion Tracking, Motion Compensation, Image Registration, Image Integration, Enhanced Reality

# Acknowledgements

First and foremost, thank you to my supervisor Dr. Terry Peters for your guidance, support and wisdom throughout this process. Your dedication to our lab and contributions to the field of medical imaging are truly inspiring.

I also thank Dr. Stephen Pautler, Dr. Hanif Ladak, and Dr. Charles McKenzie, for your advice and encouragement as my advisory committee.

Last, but certainly not least, thank you to my parents for unconditional love and support to get to where I am today and for your continued encouragement as I continue to reach for my goals. This thesis is dedicated to you.

# Contents

<b>Certificate of Examination</b>	<b>ii</b>
<b>Abstract</b>	<b>iii</b>
<b>Acknowledgements</b>	<b>iv</b>
<b>List of Figures</b>	<b>vii</b>
<b>List of Tables</b>	<b>x</b>
<b>List of Appendices</b>	<b>xi</b>
<b>1 INTRODUCTION</b>	<b>1</b>
1.1 BACKGROUND AND RESEARCH MOTIVATION . . . . .	1
1.1.1 Worldwide Statistics . . . . .	1
1.1.2 Background and History of Prostate Cancer . . . . .	2
1.2 Diagnostic Tests . . . . .	9
1.2.1 Digital Rectal Examination . . . . .	9
1.2.2 Prostate Specific Antigen . . . . .	9
1.2.3 Gleason Score . . . . .	11
1.3 Treatment Options for Prostate Cancer . . . . .	11
1.3.1 Watchful Waiting . . . . .	11
1.3.2 Hormone Therapy . . . . .	12
1.3.3 Radiation Therapy . . . . .	12
1.3.4 Brachytherapy . . . . .	13
1.3.5 Cryotherapy . . . . .	14
1.3.6 Trans-rectal High Intensity Focused Ultrasound (HIFU) . . . . .	14
1.3.7 Prostatectomy . . . . .	15
1.3.8 Laparoscopic Radical Prostatectomy . . . . .	16
1.3.9 Why Robot-assisted Laparoscopic Radical Prostatectomy . . . . .	16
1.3.10 Technical Aspects . . . . .	17
1.3.11 Steps of Laparoscopic Radical Prostatectomy . . . . .	17
1.4 Robot-Assisted Laparoscopic Radical Prostatectomy & Image Guided Surgery .	23
1.5 Previous Works . . . . .	24
1.6 Thesis Objectives . . . . .	25
1.7 Proposed Image Guidance Workflow . . . . .	26

1.8	Thesis Outline . . . . .	26
<b>2</b>	<b>TRACKING USING 2D-TO-3D ULTRASOUND IMAGE REGISTRATION</b>	<b>28</b>
2.1	Introduction . . . . .	28
2.2	Materials and Methods . . . . .	30
2.2.1	Phantom Preparation . . . . .	30
2.2.2	US Probe Calibration and 3D Free-hand Reconstruction . . . . .	31
2.2.3	Registration of 2D Intra-resection US into Pre-resection 3D TRUS . . . . .	31
2.2.4	Experiment Setup and Validation . . . . .	33
2.3	Results . . . . .	35
2.4	Discussion . . . . .	37
2.5	Conclusion . . . . .	38
<b>3</b>	<b>PROSTATE MOTION TRACKING USING SURFACE MARKERS</b>	<b>39</b>
3.1	Introduction . . . . .	39
3.2	Camera Models and Calibration . . . . .	40
3.2.1	Camera Model . . . . .	40
3.2.2	Distortion Model . . . . .	41
3.2.3	Radial Distortion . . . . .	41
3.2.4	Tangential Distortion . . . . .	42
3.2.5	Homography . . . . .	45
3.2.6	Endoscopic Camera Calibration . . . . .	46
3.2.7	Endoscope Calibration Matrix . . . . .	46
3.2.8	Triangulation . . . . .	47
3.3	Methodology . . . . .	48
3.3.1	Calibration Matrix Measurement . . . . .	48
3.3.2	Triangulation Accuracy in Different Depths . . . . .	48
3.3.3	Phantom Development . . . . .	50
3.3.4	Surface Marker Detection . . . . .	52
3.3.5	Alignment Method . . . . .	52
3.3.6	Validation . . . . .	54
3.4	Results . . . . .	56
3.5	Conclusion . . . . .	58
<b>4</b>	<b>SUMMARY SUGGESTIONS AND FUTURE WORK</b>	<b>60</b>
	<b>Bibliography</b>	<b>66</b>
<b>A</b>	<b>Copyright Use Permission</b>	<b>70</b>
	<b>Curriculum Vitae</b>	<b>72</b>

# List of Figures

1.1	Prostate and surrounding glands. . . . .	2
1.2	Zones of prostate. . . . .	3
1.3	a) Whole view of the penis, bladder, rectum, and prostate. b) Neurovascular bundles next to the prostate. . . . .	4
1.4	Endopelvic fascia between the prostate and pubic bones. . . . .	5
1.5	Levator fascia covers prostate surface. . . . .	5
1.6	Top) Pelvic plexus. Bottom) Prostatic plexus and vesicle plexus. Bottom) Prostatic plexus and vesicle plexus two major components of pelvic plexus. . . . .	6
1.7	Top) Proximal neurovascular plate. Bottom) Neurovascular bundle. . . . .	7
1.8	Levator fascia, prostatic fascia, and denonvillier fascia are bounding membranes of neurovascular bundles (a.k.a neurovascular triangle.) . . . . .	7
1.9	Apical view of the prostate containing pubic bones and puboprostatic ligaments. . . . .	7
1.10	Vas deferens and seminal vesicle close to the base of the prostate gland. . . . .	8
1.11	Fibromuscular retrotrigonal layer. . . . .	8
1.12	Top) Patient position during DRE. Bottom) Digital rectal examination. . . . .	10
1.13	Gleason scoring system based on shape of the cancerous cells. . . . .	12
1.14	HIFU: high intensity focused ultrasound probe ablating emitting ultrasound vibrations through rectal wall (RW) to ablate target tissue (hatched area A) inside the prostate gland (PR). . . . .	15
1.15	Patient positioning for RARP. . . . .	19
1.16	Separation of the bladder neck from the prostate. . . . .	19
1.17	Retrotrigonal layer is incised to expose the vasa deferentia and seminal vesicles. . . . .	20
1.18	Excision of the vasa deferentia and seminal vesicles. . . . .	20
1.19	Fixation of seminal vesicles and vasa deferentia to the prostate base. . . . .	20
1.20	Incising denonvillier fascia. . . . .	21
1.21	Incision of the blood vessels at the apex of the prostate. . . . .	21
1.22	Levator fascia is incised to expose neurovascular bundles. . . . .	21
1.23	Cutting ligaments from prostate (PR) and pubic bones (PB). . . . .	22
1.24	Location of the Foley catheter after cutting the urethra relative to prostate (PR), urethral sphincter (SPH), dorsal venous complex (DC), and urethra (U). . . . .	22
2.1	The stages of the integration of the laparoscopic video with pre-operative MRI. . . . .	29
2.2	a) Representation of a needle in 3D TRUS. 3D orthogonal planes have been adjusted to visualize the entire needle. b) Points in 2D TRUS slices corresponding to their homologies in the 3D TRUS image. . . . .	30
2.3	Point-to-line registration algorithm. . . . .	32



2.4	a) Experiment configuration for 2D to 3D TRUS image registration. b) The ultrasound probe was rotated inside the mimicked rectum assuming the TRUS probe is transverse to image plane. . . . .	34
2.5	Pixel registration error for each pixel in the moving image. . . . .	34
2.6	Registration error for different rotation angles of the beam in the simulated rectum. . . . .	36
2.7	Bright dots representing needles in 2D TRUS images for angles ranging from 40° to 90°. Note that the TRUS prob is at the top looking downwards. . . . .	36
2.8	Point-to-line registration in Aatami® augmented reality environment. . . . .	37
3.1	Pinhole camera model. . . . .	40
3.2	Projection relation in pinhole camera model. . . . .	41
3.3	Square corners become less sharp with a curved shaped where they are far from the center of the image. . . . .	42
3.4	Pattern of radial distortion at different areas of a sample image. Arrows show the distance from the correct position to the distorted coordinate of the corresponding pixel. . . . .	43
3.5	Tangential distortion pattern in pixel coordinate system for a sample image. Arrows start from the true location of the pixel to the distorted coordinate of the same pixel. . . . .	44
3.6	Triangulation of the points . . . . .	47
3.7	Experimental configuration for 3D triangulation of the checkerboard corners in different depths (top). Laparoscopic views of the detected checkerboard corners in depths 55, 110, 150, and 185mm from left to right (bottom). . . . .	49
3.8	Triangulation error(mm) for corners of checkerboard pattern in different depths using stereoscopic laparoscope. Triangulation error is less than 3.5mm for corners less than 100mm far from optical origin. . . . .	50
3.9	a) Prostate phantom (green arrow), divots (yellow arrows), and passive optical marker (red arrow), surface markers (blue). b) Spherical targets, Teflon® beads implanted inside the phantom as shown in CT. . . . .	51
3.10	colour-coded spherical features for on-line feature detection in endoscopic video. . . . .	51
3.11	Feature extraction and identification of surface markers in endoscopic view of the prostate phantom. . . . .	53
3.12	Tracking of the prostate motion using surface markers. . . . .	55
3.13	Experiment configuration. . . . .	56
3.14	Two representative fused views of the laparoscopic cameras and 3D image volume (in ortho-plane representation) showing surface markers (green spheres) and implanted targets(red spheres). . . . .	57
4.1	Relative position of the endoscopic camera and 3D image of the phantom in virtual reality environment. . . . .	61
4.2	Visual assessment of transparent view of the stereo endoscope overlaid with 3D image of the phantom (Top) versus partial occlusion of the 3D image with stereo endoscopic camera (Bottom). a) and b) can be used for “cross-eye view”; b) and c) columns can be used for “wall-eye view”. . . . .	62

4.3	Relative position of the endoscopic camera and DCE MRI of a prostate in virtual reality environment. . . . .	63
4.4	Visual assessment of transparent view of the stereo endoscope overlaid with DCE MRI (top) versus partial occlusion of DCE MRI with stereo endoscopic camera (bottom). a) and b) can be used for “cross-eye view”. b) and c) columns can be used for “wall-eye view”; . . . . .	63

# List of Tables

2.1	Fiducial localization error (FLE) for every $10^\circ$ for 2D ultrasound slices. . . . .	35
3.1	TRE for different amount of translation in AP, LR, and SI directions. . . . .	57
3.2	TRE for different rotation angles around AP, LR, and SI directions. . . . .	58
3.3	Elapsed time for different steps of image-based stereo-tracking. . . . .	58

# List of Appendices

Appendix A Copyright Use Permission . . . . . 70

# Chapter 1

## INTRODUCTION

### 1.1 BACKGROUND AND RESEARCH MOTIVATION

#### 1.1.1 Worldwide Statistics

Cancers are named after the part of the body where they start. Prostate cancer (PCa) occurs when cells in the prostate start to grow uncontrollably. PCa is the second most common cancer among Western males, with one in 7 developing the disease during his lifetime (the risk is highest after age 60), and one in 28 dying of it. Morbidity rates exist in spite of the fact that PCa is curable at early stages with survival rate of therapy being over 96% [1]. In general, men with prostate cancer have several small tumors in the prostate. Prostate cancer is very curable at early stages when all cancerous cells are within the prostate (cure rates of 90% or better) with surgery or radiation. Without regular diagnostic testing such as prostate specific antigen (PSA) and digital rectal examination (DRE), it is very difficult to find early stage prostate cancer [2].

If it is not diagnosed in a timely fashion, it can spread to surrounding organs and produce secondary tumours (metastases). At this point, the chances of a cure are much lower. Prostate

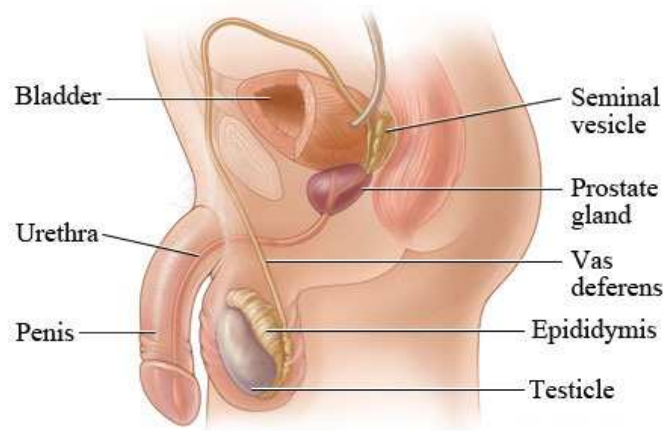


Figure 1.1: Prostate and surrounding glands.

cancer can spread to any part of the body but common areas for spread are bones and lymph nodes. Fortunately, prostate tumours grow relatively slowly, and it usually takes years for tumours to become large enough to be detectable and even longer for them to spread out of the prostate. However, small number of men have aggressive prostate cancers that grow and spread quickly. At diagnosis, it is difficult to find out which category a patient falls into and this can make treatment decisions hard.

### 1.1.2 Background and History of Prostate Cancer

**Prostate Anatomy** A healthy human prostate is classically said to be slightly larger than a walnut. The mean weight of the “normal” prostate in adult males is about 11 grams, usually ranging between 7 and 16 grams [3]. It surrounds the urethra just below the urinary bladder and can be felt during a rectal exam [4]. It is the only endocrine organ located in the midline in humans and similar animals. The prostate secretes an alkaline white fluid that constitutes 20-30% of semen along with spermatozoa and seminal vesical fluid. Spermatozoa are produced by the testes (see Figure 1.1). The prostate gland contains some smooth muscle tissue that helps expel semen during ejaculation. To work properly, the prostate needs male hormones (androgens), which are responsible for male sex characteristics.

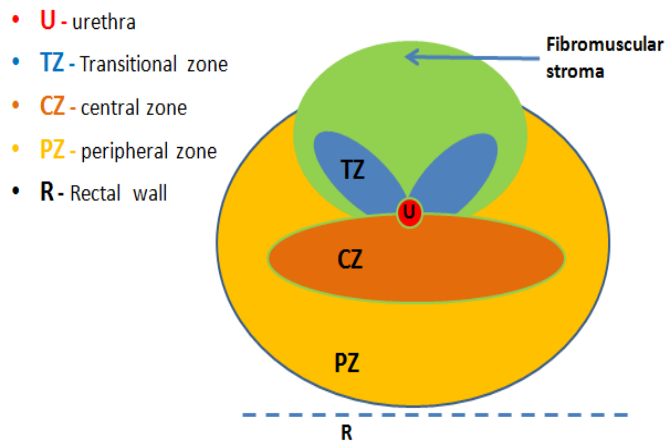


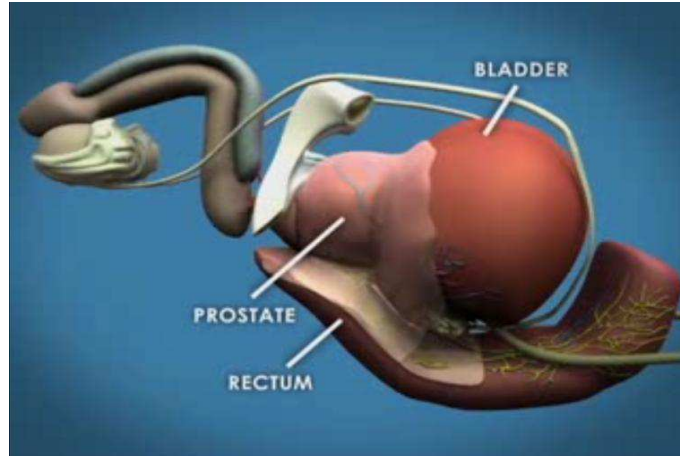
Figure 1.2: Zones of prostate.

**Prostate Zones** The prostate is split into four specific zones in terminology of pathology [5]. (see Figure1.2)

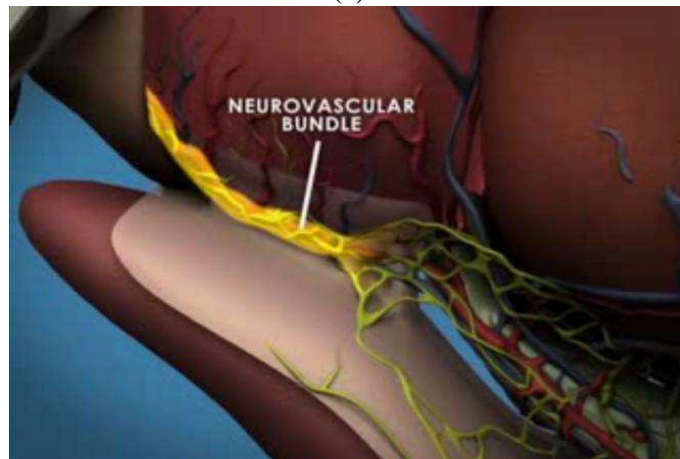
- **Peripheral zone (PZ):** constitutes up to 70%, sub-capsular portion of the posterior aspect of the prostate gland that surrounds the distal urethra. It is from this portion of the gland that 70-80% of prostatic cancers originate.
- **Central zone (CZ):** Approximately 25% normally, aggressive cancer happens in this zone. Fortunately, this accounts for only 2.5% of the prostate cancer.
- **Transition zone (TZ):** 5% at puberty, this zone accounts for 10–20% of prostate cancer and it surrounds the proximal part of the urethra.
- **Anterior fibro-muscular zone (or stroma):** This part of the prostate gland does not contain glandular tissue and composed of muscle and fibrous tissue.

**Neurovascular Bundles (NVBs)** NVBs contain both the nerve fibers and arteries that are crucial to the sexual response of the penis and they descend from posterior to the seminal vesicles and converge at the mid-prostatic level, and then diverge to fibers close to the apex of the prostate (See Figure 1.3) [6].

### Other Surrounding Tissues



(a)



(b)

Figure 1.3: a) Whole view of the penis, bladder, rectum, and prostate. b) Neurovascular bundles next to the prostate.



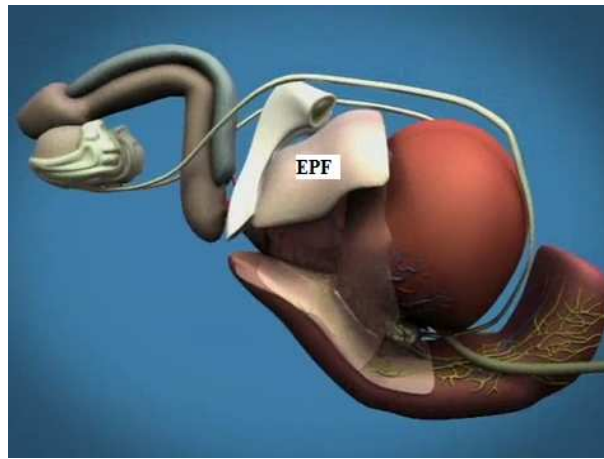


Figure 1.4: Endopelvic fascia between the prostate and pubic bones.

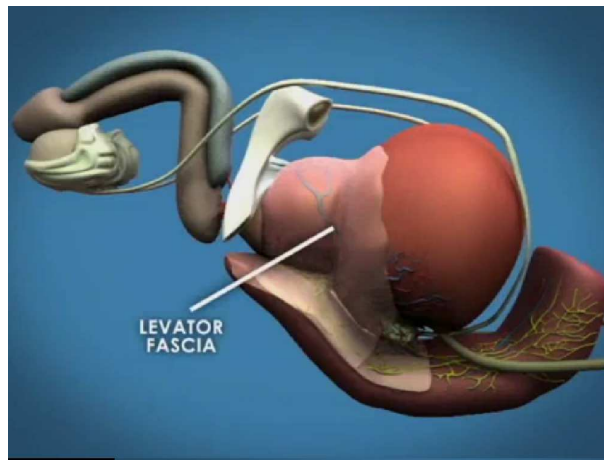


Figure 1.5: Levator fascia covers prostate surface.

**Endopelvic Fascia:** a membrane connecting pubic bones and prostate.<sup>1</sup> (See Figure 1.4)

**Levator Fascia:** covers prostate between the bladder-prostate plane.(see Figure 1.5).

**Pelvic Plexus<sup>2</sup>:** is found on the anti lateral aspect of the rectum (see Figure 1.6). Important erectile components of pelvic plexus are prostatic plexus, vesicle plexus, and interconnecting nerve fibers. These ganglions and nerve cells form the proximal neurovascular plate which can be injured during dissection of the seminal vesicles (see Figure 1.7). Neurovascular plates coalesce to form neurovascular bundles (see Figure 1.7 bottom). More clearly, neurovascular

---

<sup>1</sup>A fascia is a layer of fibrous tissue.

<sup>2</sup>Plexus means a network of anastomosing or interlacing blood vessels or nerves

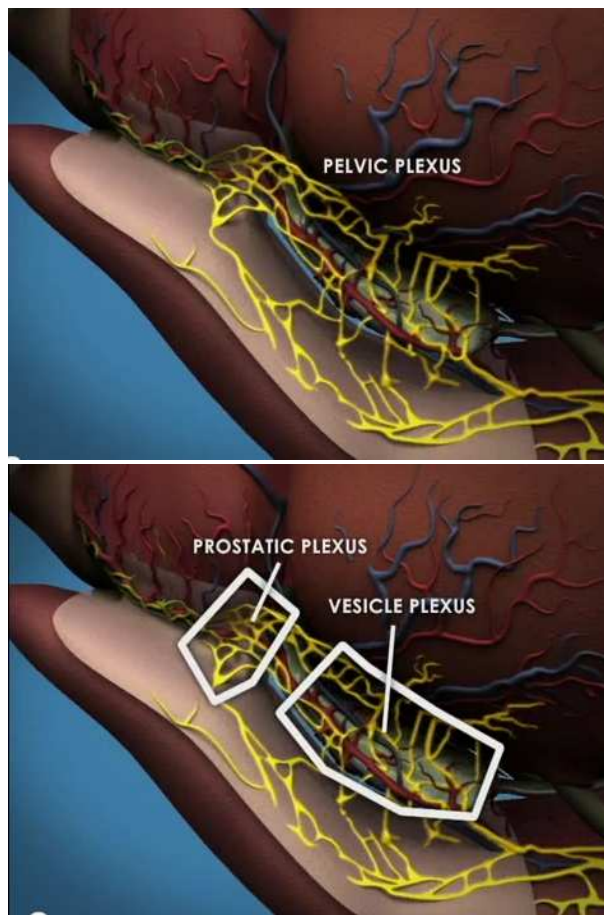


Figure 1.6: Top) Pelvic plexus. Bottom) Prostatic plexus and vesicle plexus. Bottom) Prostatic plexus and vesicle plexus two major components of pelvic plexus.

bundles are located between levator fascia, prostatic fascia, and denonvillier’s fascia. This region is called neurovascular triangle (see Figure 1.8).

**Puboprostatic ligament:** The puboprostatic ligament is a thickening of the superior fascia of the pelvic diaphragm in the male that extends laterally from the prostate to the tendinous arch of the pelvic fascia and continues forward and medially from the tendinous arch to the pubis. (see Figure 1.9)

**Seminal Vesicles:** The seminal vesicles secrete a significant proportion of the fluid that ultimately becomes semen. (see 1.10)

**Vasa Deferentia:** The vas deferens (plural: vasa deferentia), also called ductus deferens,

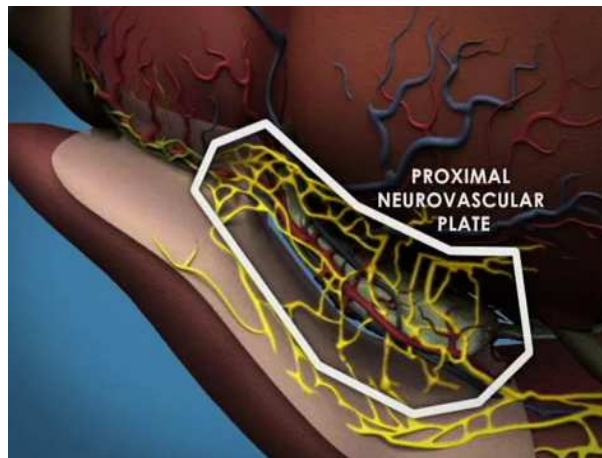


Figure 1.7: Top) Proximal neurovascular plate. Bottom) Neurovascular bundle.

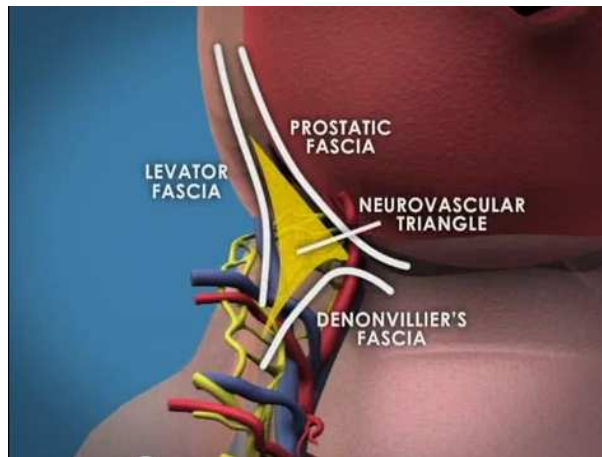


Figure 1.8: Levator fascia, prostatic fascia, and denonvillier fascia are bounding membranes of neurovascular bundles (a.k.a neurovascular triangle.)

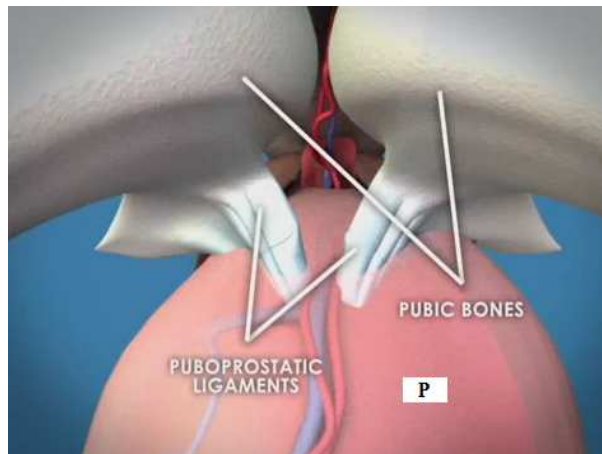


Figure 1.9: Apical view of the prostate containing pubic bones and puboprostatic ligaments.

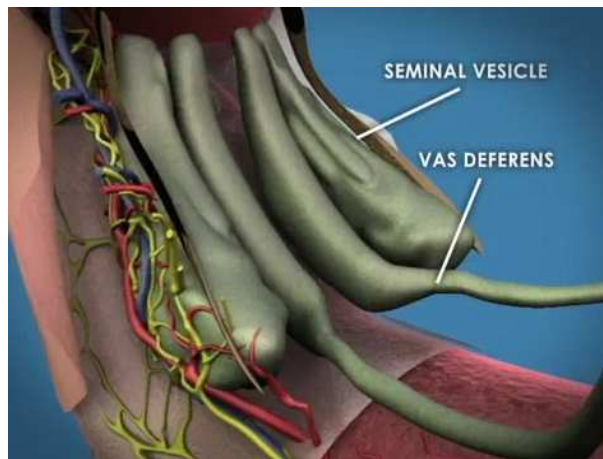


Figure 1.10: Vas deferens and seminal vesicle close to the base of the prostate gland.

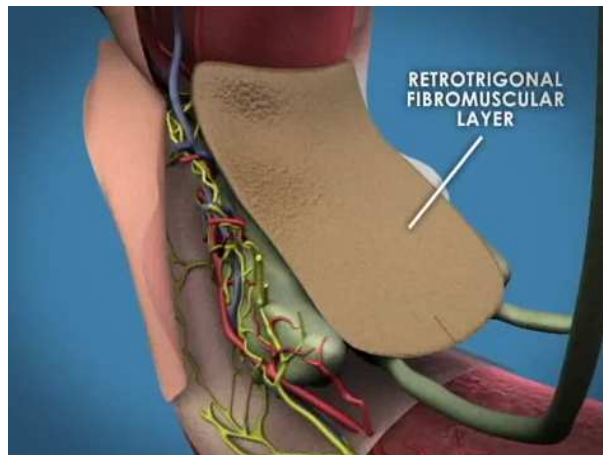


Figure 1.11: Fibromuscular retrotrigonal layer.

(Latin: “carrying-away vessel”; plural: ductus deferentes), is part of the male anatomy of many vertebrates; they transport sperm from the epididymis in anticipation of ejaculation (see Figure 1.10).

## **1.2 Diagnostic Tests**

### **1.2.1 Digital Rectal Examination**

A digital rectal examination (DRE) is the initial procedure performed to diagnose prostate cancer. The patient is asked to either bend over the examination table or lay on his left side with his knees drawn up toward his chest, and a lubricated finger is inserted through the patient's rectum (see Figure 1.12). The physician detects the irregularities of the prostate gland by touching the rectal wall, which is in direct contact with the prostate gland. Abnormalities such as hard lumps are detected as regions with stiffer characteristics than surrounding tissue as a hard lump. This test along with other symptoms (such as: decrease in urination) are indications that might suggest early stage PCa [7].

### **1.2.2 Prostate Specific Antigen**

The prostate secretes a protein, called Prostate Specific Antigen (PSA) that can be used to diagnose prostate cancer. The PSA test measures the level of the PSA in a blood sample drawn from the patient. Since analysis PSA is produced by the body, it is considered as a biological marker or a tumor marker.

PSA test is known to have relatively high false-positive rates. As an example, the PSA level can increase due to enlargement of the prostate gland that accompanies age. Although PSA is not an accurate test to detect prostate cancer and sometimes it can lead to over-diagnosis, it is very important as changes in the PSA still provide valuable information and can catch changes before they progress significantly. In addition, most of the time PSA is performed along with DRE so that the doctor can note any physical abnormalities [7].

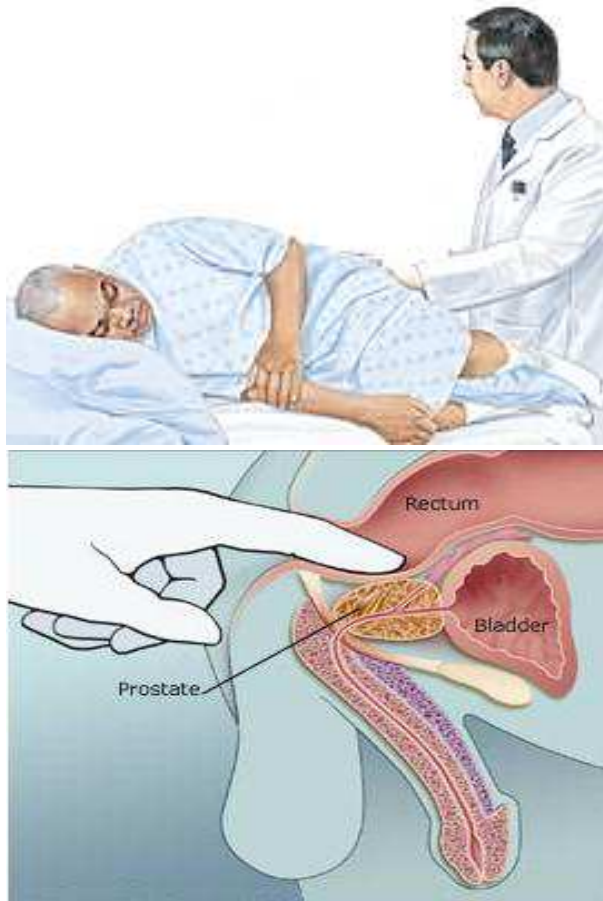


Figure 1.12: Top) Patient position during DRE. Bottom) Digital rectal examination.

### **1.2.3 Gleason Score**

The Gleason score is one means of staging prostate cancer and is named after the pathologist who proposed the method. Sample tissues are extracted via biopsy and then they are prepared as microscope slides. The pathologist assigns a grade (1-5) to the most common tumor pattern, and a second grade to the next most common tumor pattern.

Grade 5 is the most suspicious pattern extracted during the biopsy procedure. If the suspicious cells are not very different, they are well-differentiated and the associated grade would be a small number. However, if cancerous cells look very different than normal prostate cells (poorly-differentiated) the Gleason grade is assigned to be a higher value (depending on the shape of the cells, See Figure 1.13). The two grades are added together to obtain a Gleason Score in the range of 2-9 [7].

## **1.3 Treatment Options for Prostate Cancer**

### **1.3.1 Watchful Waiting**

Many prostate cancers are not aggressive and tumors grow very slowly. In most of these cases, the life expectancy of the patient is almost the same as healthy males. Therefore, some physicians do not prescribe any treatment, recommending watchful-waiting instead whereby the patient does not consume any medication or drug; however, diagnostic tests (such as: PSA or needle biopsies) are taken regularly to ensure the tumor is still benign. The same protocol is followed until aggressive progression of the tumor is detected [8].



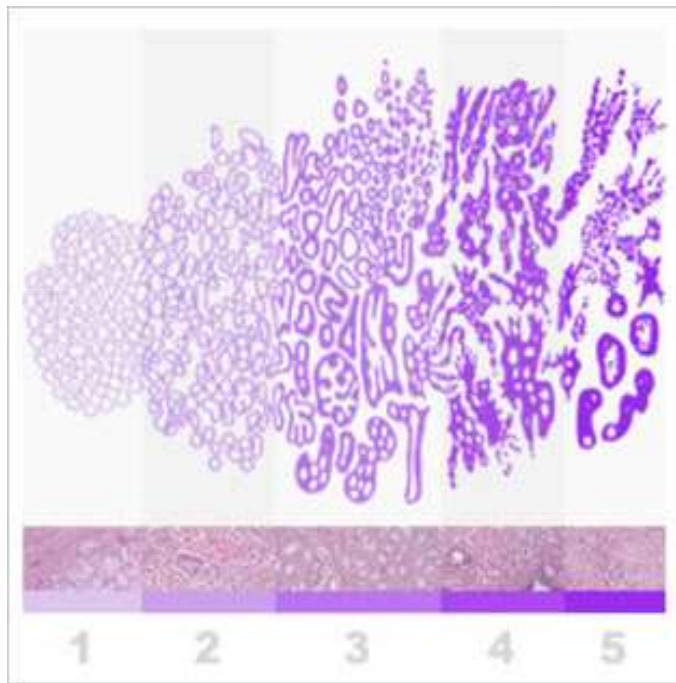


Figure 1.13: Gleason scoring system based on shape of the cancerous cells.

### 1.3.2 Hormone Therapy

Hormone therapy is systematic treatment particularly suited for cancerous cells that grow outside the prostate capsule, and treats the whole body rather than a specific area. Hormone therapy works by depriving prostate cancer cells of the male hormones (androgens) that they need to grow and flourish. This androgen deprivation can be accomplished surgically, through the removal of the testicles, or by using medication that prevents the production of androgens or blocks their effect on prostate cells.

### 1.3.3 Radiation Therapy

There are two types of radiation treatment for prostate cancer: external beam radiation therapy and brachytherapy, with the former being the older method. In the last decade, radiation physicists have refined the techniques of external beam radiation therapy (EBRT) by development of three dimensional conformal radiotherapy (3D-CRT), using numerous high-energy



photon fields, and computer software to integrate computed tomography images of the patient's anatomy. This enables the volume receiving the high dose to “conform” more accurately to the shape of the tumour. More recently, intensity modulated radiation therapy (IMRT) has become available, which allows further refinements of 3D-CRT. IMRT is an advanced form of 3D-CRT that more precisely targets a high dose of radiation to the prostate, while excluding the surrounding normal tissue as much as possible, which may further reduce toxicity.

The volume irradiated includes the prostate and part or all of the seminal vesicles depending on the calculated risk of involvement. Treatment is usually conducted 5 times a week, delivering 1.8-2 gray (Gy) daily to a total dose of 70-78 Gy. Each treatment session lasts approximately 10-20 minutes. The value of irradiation of the pelvic lymph nodes is controversial, and there is currently no indication to do this in localized disease [9].

#### **1.3.4 Brachytherapy**

Brachytherapy or seed therapy is a radiation therapy technique used as a treatment for prostate cancer. It is delivering high amount of dose to diseased tissue.

There are two types of Brachytherapy that are used in the treatment of prostate cancer: permanent low dose radiation (LDR) and temporary high dose radiation (HDR). LDR Brachytherapy uses iodine-125 (a radioisotope of iodine) and palladium-103 (a radioisotope of palladium) stored in titanium cases, usually referred to as Brachytherapy seeds. As the name “permanent Brachytherapy” suggests, the seeds are permanently left inside the prostate gland. Over the course of their radioactive lives (half-life for iodine is 60 days, and 17 days for palladium), the seeds will continuously emit low levels of radiation.

HDR Brachytherapy uses a single radioactive seed made of iridium-194 (Half-life is very short, 19 hours.) which is sometimes referred to as an iridium wire. Soft flexible plastic catheters are inserted through the perineum and into the prostate gland. HDR Brachytherapy entails an

overnight stay in the hospital during which a patient undergoes two or three treatments with the wire through each catheter.

### **1.3.5 Cryotherapy**

Cryotherapy (a.k.a cryoablation and cryosurgery) is a relatively new treatment whereby diseased tissue undergoes freeze-thaw cycles to destroy cancerous cells. Consecutive freeze-thaw cycles create ice crystals inside and outside of the cells, destroy cells through dehydration, and drastic change in pH<sup>3</sup> level. In addition, it activates tumour anti-bodies to eradicate the tumour [10].

Due to the lack of long-term studies on the results of Cryotherapy, radiation therapy is considered as the preferred option. However, for cases where tumours are radio-resistant Cryotherapy is considered as a more effective replacement [10].

### **1.3.6 Trans-rectal High Intensity Focused Ultrasound (HIFU)**

HIFU was introduced first in early 1990. In the first application it was employed under endoscopic guidance. In principle, the idea is to focus the high intensity ultrasound on the target point. The concentration of ultrasound vibrations increases the temperature of the target dramatically (up to 80°C) coagulating the target tissue (13mm in width, 520mm in height) so in order to destroy the entire tumour, it is necessary to place elementary focal lesions side-to-side throughout the targeted tumour volume [11] (see Figure 1.14).

---

<sup>3</sup>Measure of the acidity or basicity of an aqueous solution

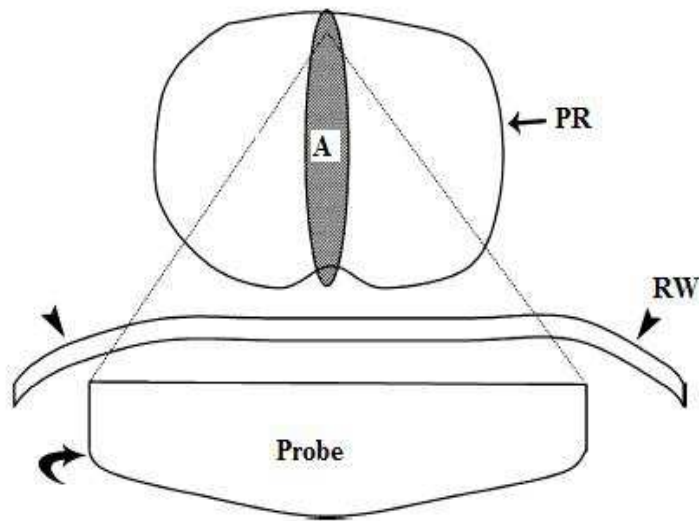


Figure 1.14: HIFU: high intensity focused ultrasound probe ablation emitting ultrasound vibrations through rectal wall (RW) to ablate target tissue (hatched area A) inside the prostate gland (PR).

### 1.3.7 Prostatectomy

Prostate surgery is the removal of the prostate gland along with all cancerous cells developed inside the prostate. Prostatectomy is the technical word usually used for it. There are three types of prostatectomy

- **Retropubic:** The patient's abdomen is incised around the pubic bones (incision size is around 8-10cm, depending on the size of the patient). The patient has a better chance for nerve sparing in this type of prostatectomy.
- **Perineal:** An incision is made between the anal sphincter and scrotum (4cm length). The assumption is that PSA testing, Gleason score, and DRE are all indicative of aggressive cancer.
- **Laparoscopic and Robotic:** In this approach laparoscopic camera is introduced into the abdominal cavity to observe laparoscopic instruments and the prostate at close range while the procedure is performed. This allows the surgeon to perform the surgery through

few small incisions (via a trocar) rather than a long incision; and therefore it reduces patient trauma. Extraperitoneal and transperitoneal are two common methods to reach to the prostate gland. The former uses a peropertoneal space to access the bladder and prostate excision is performed subsequently after dissection of the bladder neck.

### **1.3.8 Laparoscopic Radical Prostatectomy**

Laparoscopic Radical Prostatectomy (LRP) is the most demanding laparoscopic surgery in urology that has been established as the standard method for localized prostate cancer [12]. The major advantages of LRP are lower intra-operative bleeding and lower postoperative pain, a shorter period of urethral catheterisation, and shorter hospital stay.

### **1.3.9 Why Robot-assisted Laparoscopic Radical Prostatectomy**

LRP was supposed to reduce blood loss and shorten operating room times and hospital stays, while attaining functional outcomes similar to open radical prostatectomy (ORP). Despite these advantages, LRP was proved to be a complex procedure constrained by two dimensional visualization that led to a steep learning curve in addition to limited ergonomics. For example, maneuvering a rigid laparoscope fixed at the skin level requires greater skill compared to open surgery. Robot-assisted laparoscopic radical prostatectomy (RARP) was invented to overcome some of these difficulties. In early 2000, the first robot-assisted laparoscopic radical prostatectomy was performed using the da-Vinci<sup>®</sup> Surgical System (Intuitive Surgical, Sunnyvale, CA). Since this technology is equipped with stereoscopic endoscope, it provides the 3D view of the surgical target. In addition, jointed laparoscopic tools mimic wrist-like motions providing dexterity similar to the surgeon's hands. The result is that laparoscopic dissection is performed with greater ease, operator learning curves are shorter and widespread patient and surgeon interest in minimally invasive prostatectomy has been created. Despite the extensive popularity

of RARP, there is no scientific evidence that post operative potency rates have improved noticeably compared to ORP. [13] Technically skillful surgeons ask whether the robotic instruments improve the efficiency of the procedure. For those with sufficient laparoscopic technical proficiency, the robot may not be required or, even, advantageous. However, for the majority of surgeons, robotic arms along with the laparoscopic view makes the dissection easier and highly facilitates suturing. Certainly, the transition from open to laparoscopic surgery is greatly eased by surgical robots [12].

Regardless of patient demand, the main rationale for the popularity of RARP is in improving the surgical outcomes. Comparative outcomes can be achieved as discussed below; however, improved outcomes serve as the primary basis for the establishment and development of RARP.

### **1.3.10 Technical Aspects**

Different robotic settings can be potentially employed to perform a robotic prostatectomy; however, in most of studies the application of the da Vinci surgical robot is greatly reported and recommended. This is a master/slave device wherein the surgeon is seated at a console remote from the operative table. The surgeon is able to control and manipulate the stereoscopic endoscopic camera as well as there robotic arms [12].

In the following, major steps of a typical laparoscopic radical prostatectomy procedure is described; however, the complexity of the surgery highly depends on the progression of the tumour and patient-specific anatomy of the prostate.

### **1.3.11 Steps of Laparoscopic Radical Prostatectomy**

**Patient Positioning:** First robot needs to be positioned appropriately with respect to the patient's body in the sense that it has maximum exposure to the patient's pelvis in order to en-

hance dexterity of the robotic arms (see Figure 1.15). This type of patient positioning is also called lithotomy position with steep Trendelenburg<sup>4</sup>. At the same time, the patient's arms have to be protected to avoid any conflict with the surgical robot. An "egg crate" foam pad can prevent slippage of the patient to hold the body in the Trendelenburg position. Besides, Trendelenburg positioning helps displace bowel from the pelvis when an intraperitoneal approach is used.

Determining the position of the camera port is very important as it affects the view of the surgical sight throughout the procedure. Superior to the umbilicus is usually considered the right place for this port. Additional ports are cut for robotic arms (5mm in diameter) as well as a wide port for the assistant (12mm in diameter, usually located in the right lower quadrant). It might be helpful to cut one port for the assistant if the colon tends to obscure the pelvis.

In terms of instruments, monopolar scissors are usually attached to the right arm. The left arm of the robot is usually equipped with either a grasper or bipolar forceps. The role of the side assistant is to provide suction and passage of suture and clips through the right lower quadrant 12 mm port. The fourth arm is used for retraction, and employs a serrated grasping instrument [12].

**Development of the operative field** As discussed before, there are two possible ways to reach the prostate gland, and there is not any significant difference in each of the methods according to Kirby et al. [12]. Nonetheless, the extraperitoneal approach helps isolate any urine leak from the peritoneal cavity and may help with postoperative tamponade<sup>5</sup> of bleeding. However, the working space is reported to be smaller using this approach. Most surgeons have preferred an intraperitoneal approach [12].

**Steps of the excision** First the bladder neck is identified and the prostate is separated from the bladder (see Figure 1.16). The Retrotrigonal fibromuscular layer is then identified and cut through to access the anterior aspect of the vasa deferensa and seminal vesicles. From this

---

<sup>4</sup>The body is laid in the supine position with the feet higher than the head by 15-30 degrees.

<sup>5</sup>The closure or blockage a wound or body cavity by or as if by a tampon especially to stop bleeding.

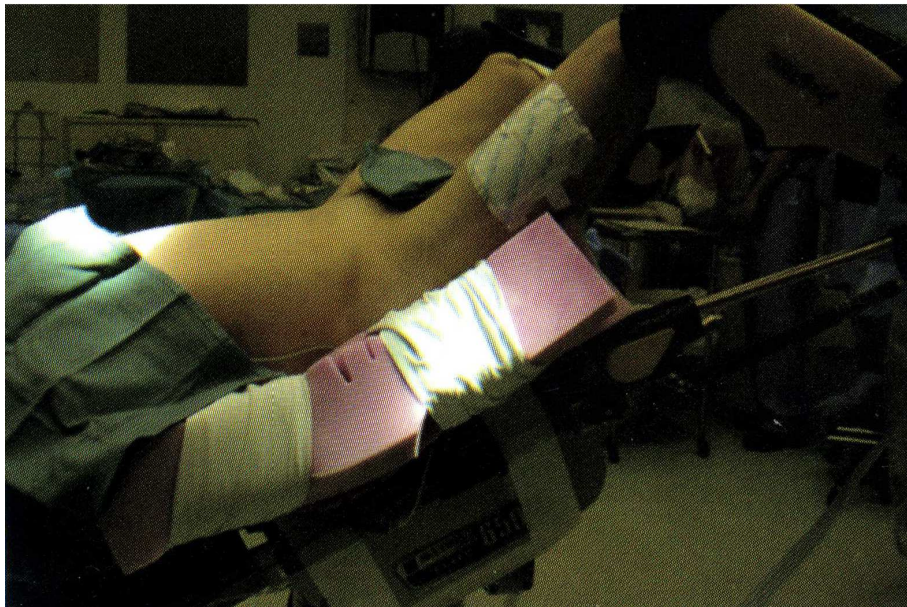


Figure 1.15: Patient positioning for RARP.

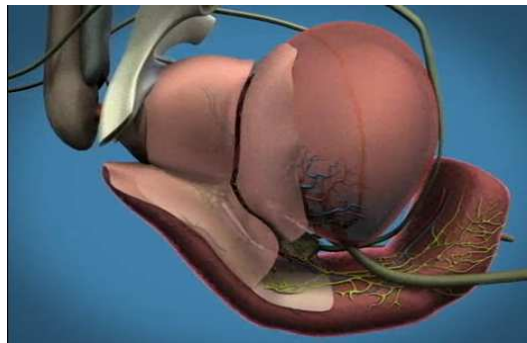


Figure 1.16: Separation of the bladder neck from the prostate.

point the surgery is performed without cautery <sup>6</sup> (see Figure 1.17). Vasa deferentia and arteries running through them are identified and secured and cut (see Figure 1.18). The separated vesicles and deferentia are then lifted up and sutured to the prostate base (see Figure 1.19). The prostate is lifted up and the denonvillier fascia is separated (see Figure 1.20).

The surgery is then followed by securing blood vessels using clips or sutures (see Figure 1.21). The prostate is then retracted to one side and an incision is made over levator fascia near the neurovascular bundle exposing the neurovascular triangle. This leads to an initial release of the neurovascular bundle and blood vessels and nerves are cut using clips at two sides of the

---

<sup>6</sup>Cutting the tissue by heat and burning.

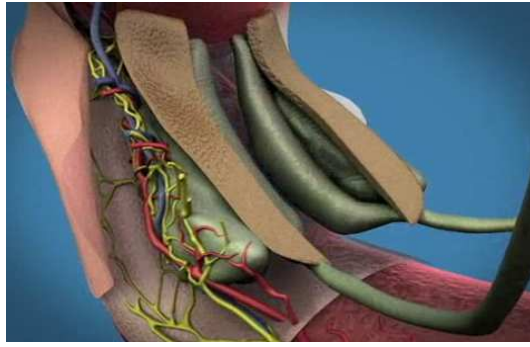


Figure 1.17: Retrotrigonal layer is incised to expose the vasa deferentia and seminal vesicles.

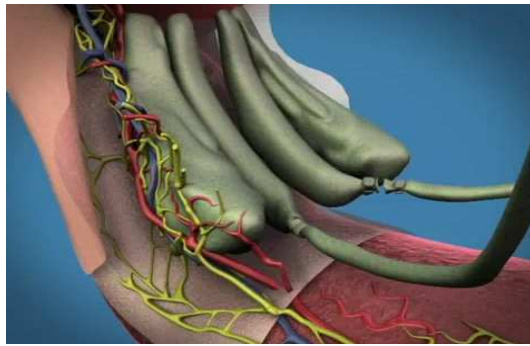


Figure 1.18: Excision of the vasa deferentia and seminal vesicles.

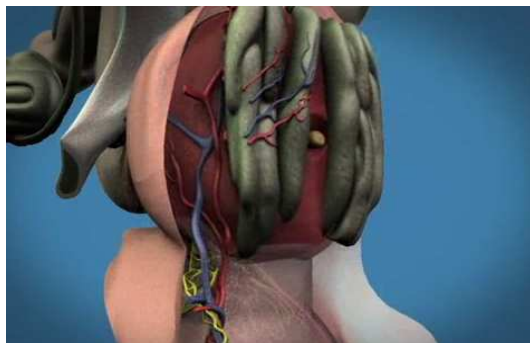


Figure 1.19: Fixation of seminal vesicles and vasa deferentia to the prostate base.



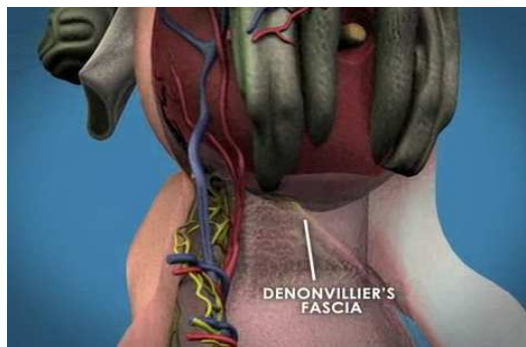


Figure 1.20: Incising denonvillier fascia.



Figure 1.21: Incision of the blood vessels at the apex of the prostate.

prostate (see Figure 1.22). In the next step, the prostate is pulled back so that puboprostatic ligaments are exposed and they can be incised close to prostate (see Figure 1.23). The Dorsal venous complex is secured and cut next and striated urinary sphincter is freed from the prostate. The urethra is cut afterwards in such a way that Foley catheter can be seen (see Figure 1.24). At this point the prostate is released to be removed from the abdominal cavity.

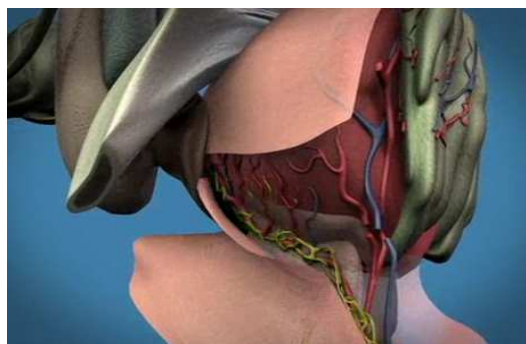


Figure 1.22: Levator fascia is incised to expose neurovascular bundles.

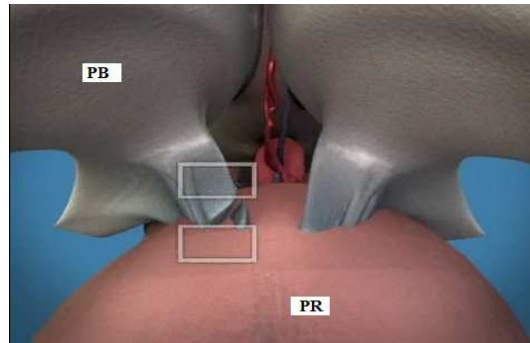


Figure 1.23: Cutting ligaments from prostate (PR) and pubic bones (PB).

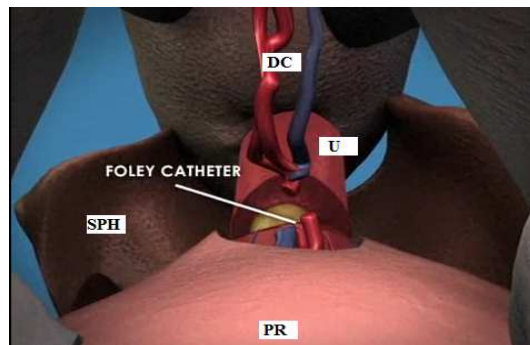


Figure 1.24: Location of the Foley catheter after cutting the urethra relative to prostate (PR), urethral sphincter (SPH), dorsal venous complex (DC), and urethra (U).

## **1.4 Robot-Assisted Laparoscopic Radical Prostatectomy & Image Guided Surgery**

Image guided intervention has improved many clinical procedures. Although the routine use of image-guided intervention (IGI) is only about 20 years old, it grew out of stereotactic neuro-surgical techniques that have a much longer history [14]. As mentioned earlier, image guided radio therapy is an example of improvement to conventional radiotherapy provided by IGI. Recently, image guided interventions have been significantly considered in urology applications such as prostate biopsy, Laparoscopic Radical Nephrectomy (LRN), and LRP [15]. In fact, the scholars believe that one important reason behind lower success of RARP might be due to the fact that the locations of cancer foci are subcutaneous even in the endoscopic view making surgeons to excise wider margins around the prostate capsule. In addition, nerve sparing is another issue that surgeons try to maximize as it highly correlates with preserving patients' potency. Fortunately, imaging techniques cannot only provide a better view of progression of the cancer, but they can also visualize NVBs located laterally next to the prostate. Dynamic Contrast Enhanced Magnetic Resonance Imaging (DCE-MRI) and computed tomography (CT) perfusion can show distribution of the new vasculature. T2 weighted imaging can provide locations of NVBs [16, 17]. Despite such valuable imaging techniques, surgeons do not have the chance to see them during the operation while the excision is being performed. In contrast if a surgeon can see them in the endoscopic view, we believe that they have the chance to decide better margins around the prostate and maximize nerve sparing in order to reduce patient impotency.

The work in this thesis describes two approaches that can be employed to intra-operatively track a fused pre-operative MR image of the prostate.

## 1.5 Previous Works

Dynamic Contrast Enhanced (DCE) MRI and T2 weighted MRI have the potential to assist in the diagnosis of cancer in the prostate and image the three dimensional distribution of the tumour [17]. However, the efficacy of such MR imaging to guide the surgeon is reduced unless it is fused with the prostate laparoscopic video as viewed by the surgeon during a laparoscopic prostatectomy procedure.

Cohen *et al.*[18] investigated the performance of such an image guided intervention during different stages of a typical prostatectomy procedure, by simply overlaying stationary laparoscopic images with the pre-operatively preprocessed MRI of the target tissue. The authors noted that, based on surgeons' statements, the integrated laparoscopic view is of greatest assistance for nerve sparing and mobilizing the apex of the prostate; however, since the prostate moves due to interaction with the surgical tools and patient motion, compensating for prostate motion during the procedure is an important step to maintain the alignment between the preoperative model and real-time video.

In nephrectomy, Baumhauer *et al.*[19] attempted monocular target pose estimations and navigation methods for laparoscopic partial nephrectomy. Here the authors used a mobile C-Arm and surface markers (surgical aids). However, monocular pose estimation methods are sensitive to noise due to the assumption that the geometry of the target tissue is known during the partial nephrectomy procedure.

Yip *et al.* [20] investigated registration of 3D ultrasound into a stereo camera using a registration tool attached over the air-tissue boundary describing the map between coordinate frames of two modalities. However, the usability of such tools is reduced due to the larger size than the diameter of trocar for minimally invasive abdominal surgeries. Also, possible conflicts between the registration tool, ultrasound probe, and other common surgical tools has not been investigated under usual clinical constraints [20].

Ukimura *et al.* [15] proposed optical tracking techniques to fuse 3D TRUS with laparoscopic images whereby an infrared optical tracking system was used to perform registration. However, such tracking and fusion is usable only to the point of detachment of the prostate from the rectal wall (which occurs during the process to remove the prostate). In addition, a direct line of sight must be maintained for both laparoscope and the ultrasound probe placed between patient's legs.

In TRUS-guided biopsy, De Silva *et al.* [21] have considered an image-based rigid registration technique that aligns live 2D TRUS images, acquired immediately prior to biopsy needle insertion, with the pre-acquired 3D TRUS image to compensate for intra-session prostate motion. However, robustness and the real-time computational complexities affect the suitability of this method.

## **1.6 Thesis Objectives**

The goal of this thesis is to consider integration methods to bring the pre-operative 3D image into alignment with the endoscopic frame for RARP so that surgeons know where cancer foci are relative to critical tissues (neurovascular bundles in this application). This improves the chance for preserving nerves and erectile function after the surgery which is considered one of the main outcomes of the prostatectomy procedure.

Two tracking and registration techniques are specifically investigated to dynamically compensate for prostate rotation and translation during the operation in real-time and to apply such motion to the preoperative model in order to maintain alignment.

## 1.7 Proposed Image Guidance Workflow

One of the most common and cost-effective ways to register pre-operative images (such MRI and/or CT) into the intraoperative patient coordinate system is to register 3D MRI into 3D transrectal ultrasound since ultrasound is considered a portable imaging modality compared to other imaging methods. This initial registration brings the pre-operative MRI (or CT) into the alignment with the patient coordinate system.

3D ultrasound can be acquired in two different ways, either by 3D TRUS probes or by 2D reconstruction. The first method benefits from 3D TRUS equipped with a 2D array of piezoelectric crystals. The latter method benefits from a calibrated ultrasound transducer and a tracking system (either mechanical or magnetic) recording the relative position of a set of 2D TRUS images which are being re-sampled in the next step [22, 23].

The second step after registration is the tracking of the prostate motion due to interaction with surgical tools, which can cause rigid motion and even deformation. Therefore, a tracking component seems necessary to compensate for this type of motion. Applying the tracked motion along with initial transformation allows us to register pre-operative MRI into the stereo video coordinate system. In this study, the main concern is to propose methods that can best track intra-operative rotation and translation of the prostate due to the surgical tools.

## 1.8 Thesis Outline

The rest of this thesis is organized as follows. The second chapter investigates a 2D-to-3D point to line registration algorithm to track intra-operative prostate motion and translation. Chapter 3 considers point-based stereoscopic tracking using surface markers as a more efficient technique to track the prostate motion relative to camera coordinate system. In chapter 4, I compare and contrast each of the proposed tracking methods and conclude by discussing future work to

realize integration of the endoscopic view for RARP.

# **Chapter 2**

## **TRACKING USING 2D-TO-3D ULTRASOUND IMAGE REGISTRATION**

This chapter is appended from the paper “A 2D to 3D ultrasound image registration algorithm for robotically assisted laparoscopic radical prostatectomy”, Proc. SPIE 7962, 79621Z (2011), Orlando Florida.

### **2.1 Introduction**

During a prostatectomy procedure, the tissue being resected can be rotated and translated significantly by the surgical instruments during the excision procedure. Therefore, to keep the laparoscopic video robustly fused with the pre-operative MRI, the motion and deformation of the prostate must be quantified in real-time, at least during the planning stage performed at the beginning of the procedure. Registration of acquired intra-resection 2D US with the pre-resection 3D TRUS image acquired prior to beginning the procedure (called intra-resection registration)



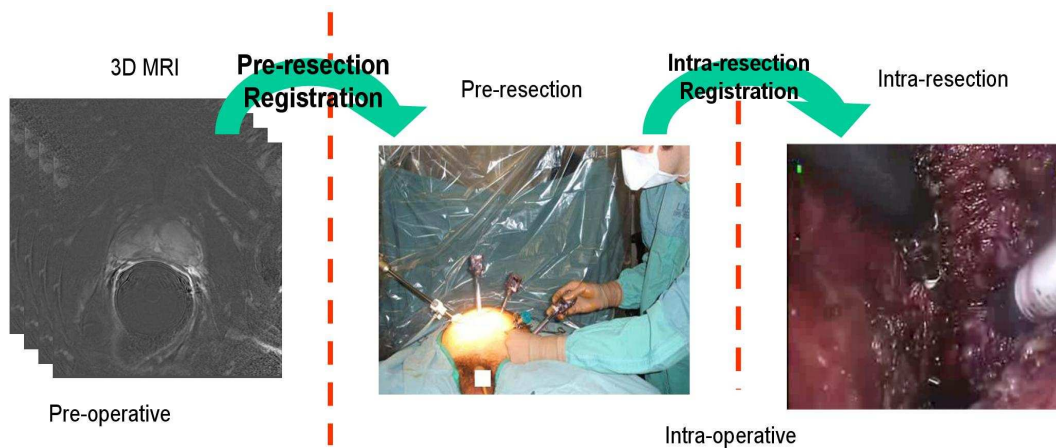


Figure 2.1: The stages of the integration of the laparoscopic video with pre-operative MRI.

is proposed to measure the prostate motion dynamically in real-time (see Figure 2.1).

A similar approach using 2D to 3D TRUS image registration also has been studied in targeted prostate biopsy to integrate the US-guided biopsy procedure with the pre-operative MRI [24]. Also, registration of the 3D-TRUS to 3D TRUS has been studied by Karnik et al.[23] for the purpose of repeat prostate biopsy to quantify accuracy of registration of 3D TRUS between biopsy sessions. In another study, Karnik et al. [25] investigated different registration methods to compensate prostate motion due to patient motion or respiration. However, one of the major issues in TRUS image registration is the limited contrast between the prostate and surrounding tissue, which diminishes the accuracy of the alignment, particularly for intensity-based registration approaches. Also, conventional surface-based registration is not performed automatically in real-time as it requires the prostate boundary to be segmented manually. In this chapter, I investigated a registration technique to address these problems, which, as an alternative to image-based registration, proposes a fiducial based approach involving the insertion of needles within the prostate as a reference structure before the resection to accelerate the alignment process. Such needle insertion is performed while the patient is under general anesthesia and is considered a feasible approach by our surgical colleagues. The inserted needles are bright in ultrasound images, and enable an acceleration of the 2D to 3D registration while maintaining the accuracy needed for image-guided RARP.

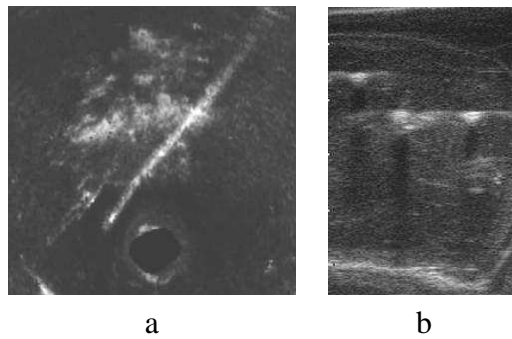


Figure 2.2: a) Representation of a needle in 3D TRUS. 3D orthogonal planes have been adjusted to visualize the entire needle. b) Points in 2D TRUS slices corresponding to their homologies in the 3D TRUS image.

## 2.2 Materials and Methods

### 2.2.1 Phantom Preparation

Different approaches have been considered to simulate the physical and imaging properties of the prostate. In the current work poly-vinyl-alcohol cryogel (PVA-C) [26] was used to mimic different tissues since its mechanical properties can be made similar to human body tissue, and can be imaged with both MRI and US. Different numbers of freeze-thaw cycles (FTC) polymerizes PVA-C such that mechanical properties of tissue can be approximated. Soto et al. [27] identified the appropriate number of FTCs to get the imaging tissue characteristics (attenuation coefficient, propagation speed, and backscatter for US; T1 and T2 relaxation times for MRI) similar to the prostate.

Three needles were inserted into a prostate phantom as reference objects. A 3D ultrasound image was then acquired as a pre-resection reference image from which the needles were segmented manually. 2D TRUS slices were then acquired in which the needles are depicted as bright points (see Figure 2.2.b). To establish a transform between the pre-resection 3D US and the 2D slices, an algorithm is proposed which finds the position of the three points in the 3D TRUS such that they are placed on needles. Then, a generalized solution of the Orthogonal Procrustes Problem, proposed by Schonemann et al. [28] and Farrell et al. [29] was used to find

the rigid transform mapping the 2D slice into its real position in the 3D space. The Procrustes algorithm is a non-iterative rapid process and is very suitable to real-time image alignment and prostate motion compensation.

### **2.2.2 US Probe Calibration and 3D Free-hand Reconstruction**

The ultrasound probe was tracked by a 6 degree-of-freedom (DOF) magnetic tracking sensor (NDI Aurora<sup>®</sup>), and phantom-less calibration provides the calibration matrix for the ultrasound beam. The calibration error using this approach has been measured at 1.16mm by Cheung et al. [30]. An open-source free hand 3D reconstruction algorithm implemented by Pace et al. [31] was applied to generate the 3D ultrasound volumes. Using this method, a the TRUS probe scans the volume of the target tissue by generating a set of 2D ultrasound images. Since the probe is tracked the relative position of the 2D slices are recorded at the same time. Then, a 3D volume containing the whole set is resampled to generate a 3D image representing the target tissue.

### **2.2.3 Registration of 2D Intra-resection US into Pre-resection 3D TRUS**

Registration of ultrasound prostate images is challenging because the ultrasound image does not provide anatomical features that are as well defined as in other modalities. Therefore, we propose to insert three needles along non-parallel trajectories as reference objects at the beginning of the procedure. These needles are bright in the reconstructed 3D TRUS images and maintain 30-45 ° degrees with respect to the left to right direction in patient coordinate (see Figure 2.2). These lines are then used as homologous structures to register 2D slices into the 3D TRUS images. During the intervention, needles are represented by three bright points in the 2D US beam. From the three lines in the pre-resection TRUS and the homologous intersection points in intra-resection slices, we obtain the transform representing the motion of the prostate

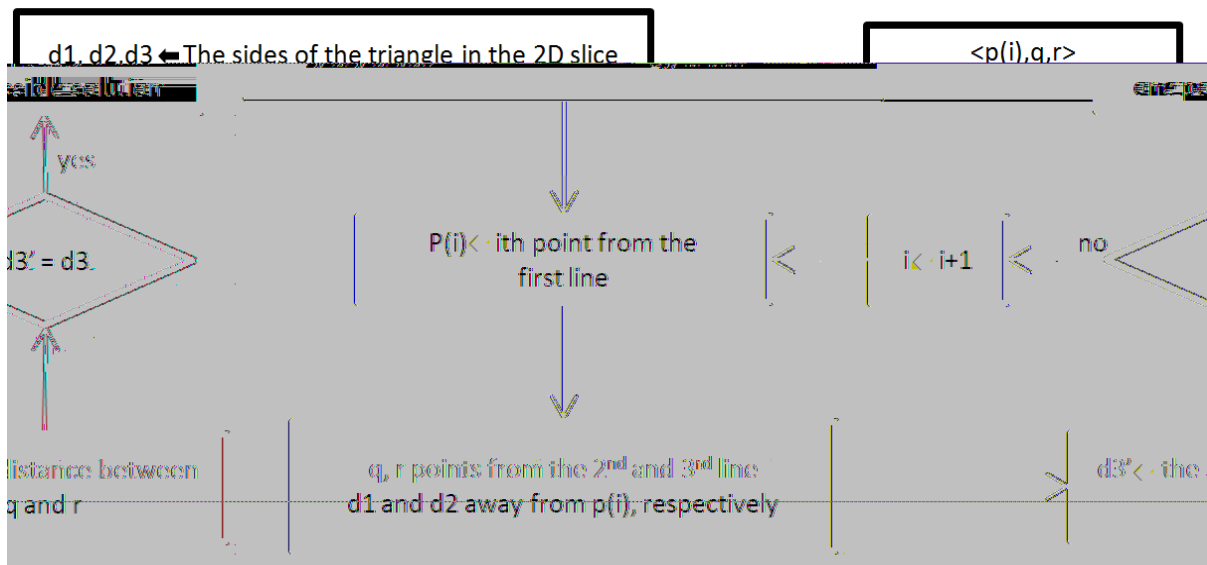


Figure 2.3: Point-to-line registration algorithm.

from its original position to its current position. The procedure is split into the following main steps after 3D reconstruction:

1. The needles as visualized in 3D TRUS are segmented into lines by selecting the ends of each line.
2. The cross-section images of the needles as seen in the 2D TRUS are selected by three points.
3. Three sides of the triangle connecting the points are calculated.
4. The position of the triangle whose vertices lie on the three lines is determined by the algorithm described in Figure 2.3, which traverses one of the lines and determines where the triangle (in the 2D slice) is possibly fitted to the lines.
5. A singular-value decomposition (SVD) point-based registration [28] quantifies the rotation and translation which bring the selected points in 2D slices into alignment with 3D reconstructed ultrasound.
6. The mutual information similarity metric is used to determine whether the pixel intensi-

ties of the 2D slice match the 3D ultrasound in the assessed position.

7. If the 2D slice does not match in the 3D image, the next possible solution is examined by going to the 4<sup>th</sup> step.

Since this approach only searches one of the lines, it runs more rapidly than image-based registration and does not suffer from the possibility of converging to a local minimum. Note that the lines must form the edges of a 3-sided pyramid, since if they are parallel, the point-to-line algorithm will find an infinite number of solutions. Also, the computational cost of this approach is lower than image-based registration because the search space has one dimension only. Notably, in practice, since the probe is rigid, its motion is limited to rotation inside the rectum and there is only one unique location where the 2D image corresponds to the 3D TRUS image. Given this constraint in practice, most of the time we can skip mutual information step which makes it much faster and suitable for tracking of the prostate in real-time during a RARP.

## **2.2.4 Experiment Setup and Validation**

Needles were inserted inside the prostate phantom and a tracked laparoscopic ultrasound probe was used as the gold standard to validate the proposed algorithm (see Figure 2.4.a). The tracked probe was rotated from 30 to 100 degrees from left to right in a clockwise direction, and a 2D slice was acquired every 5 degrees (see Figure 2.4.b). For each 2D slice, the pixel registration error (PRE) which is the distance between positions of the pixel in the 2D slice transformed by the optimum transform (measured by tracked probe), and the assessed transform using point-to-line registration (see Figure 2.5) was calculated. Then the mean of PRE (MPRE) was calculated for all of the pixels in one slice using the following equation to measure the registration error for the corresponding angle in the whole image:

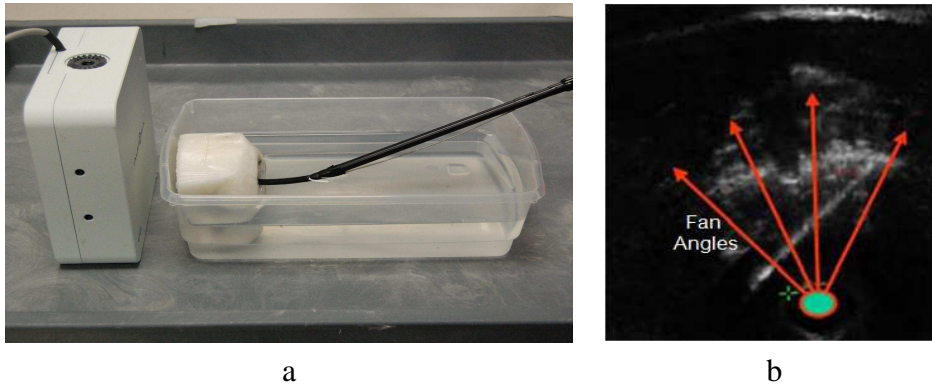


Figure 2.4: a) Experiment configuration for 2D to 3D TRUS image registration. b) The ultrasound probe was rotated inside the mimicked rectum assuming the TRUS probe is transverse to image plane.

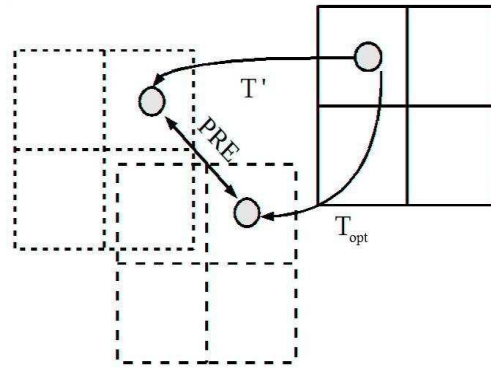


Figure 2.5: Pixel registration error for each pixel in the moving image.

$$MPRE(T') = \frac{1}{N} \sum_{p \in P_m} \|T_{opt}(p) - T'(p)\|. \quad (2.1)$$

In the above,  $P_m$  is the pixel set of the 2D TRUS,  $T_{opt}(p)$  is the optimum transform measured by the tracked probe,  $T'(p)$  is the assessed transform, and  $N$  is the number of pixels in the moving image. The voxel size for the 3D reconstructed US is 0.41x0.42x0.41mm, while the pixel size of the 2D slices is 0.21x0.21mm (acquired by Aloka<sup>®</sup> SSD-1700 7.5MHz US scanner). The US probe was tracked by an NDI Aurora<sup>®</sup> magnetic tracking system (NDI Waterloo ON, Canada).

Angle (deg.)	30	40	50	60	70	80	90	100
FLE (mm)	1.90	2.25	2.46	2.03	2.53	2.22	3.01	2.52
Std. Dev. (mm)	1.35	1.88	1.25	1.85	2.25	1.95	2.68	2.35

Table 2.1: Fiducial localization error (FLE) for every 10° for 2D ultrasound slices.

## 2.3 Results

In order to validate the accuracy of proposed registration method, we used position and orientation reported by the magnetic tracking system as a gold standard to measure 2D-3D registration error. The probe was rotated inside the simulated rectum and a 2D slice was acquired every 5 degrees. Every 2D slice was then registered into the 3D TRUS using point-to-line registration algorithm. The registration accuracy results are reported in Figure 2.6. The registration error decreases as the US fan becomes close to being transverse to the needles. The average of MPRE for all of these angles is  $2.68 \pm 1.31$ mm. Note that a clinically acceptable registration error for RARP should be less than 3-5mm (depending on the size of the patient’s prostate) based on the experience of our surgical colleagues when using the da Vinci Robotic system. Fiducial Localization Error (FLE) was calculated for every 10° for 2D ultrasound slices by selecting the position of the points five times (see Table 2.1). Since the position of the needle can only be identified with a precision of 2-3mm, this distorts the registration accuracy. A screen shot of one result of the point-to-line registration algorithm is illustrated in Figure 2.8. The 3D spheres depict the true positions of the 2D TRUS in a virtual environment, and the triangles are the positions calculated by the point-to-line registration algorithm. Finally, the point-to-line registration algorithm takes less than 50ms to find the optimal solution given the position of the lines and points in the tracking coordinate system.

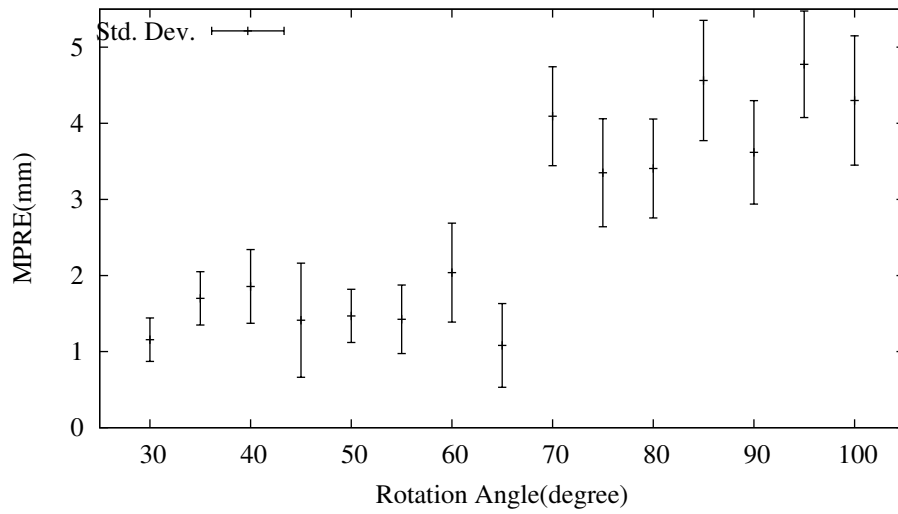


Figure 2.6: Registration error for different rotation angles of the beam in the simulated rectum.

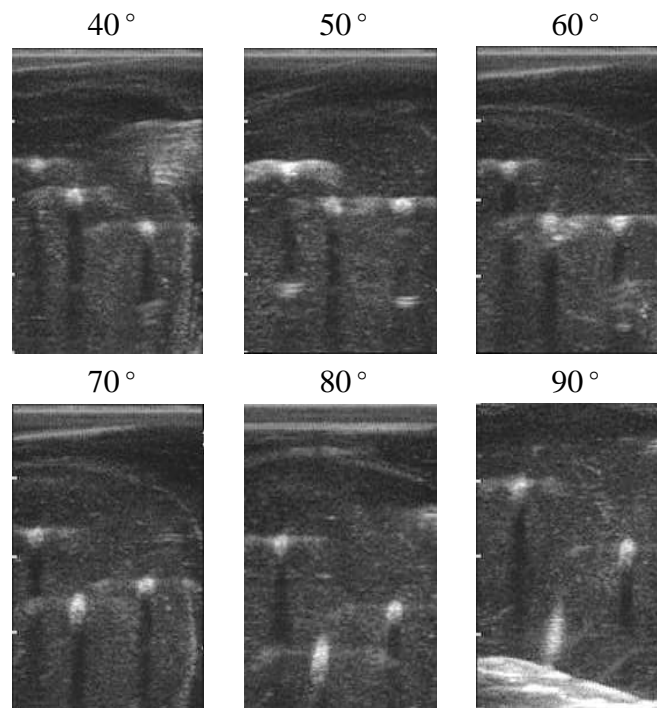


Figure 2.7: Bright dots representing needles in 2D TRUS images for angles ranging from 40° to 90°. Note that the TRUS prob is at the top looking downwards.



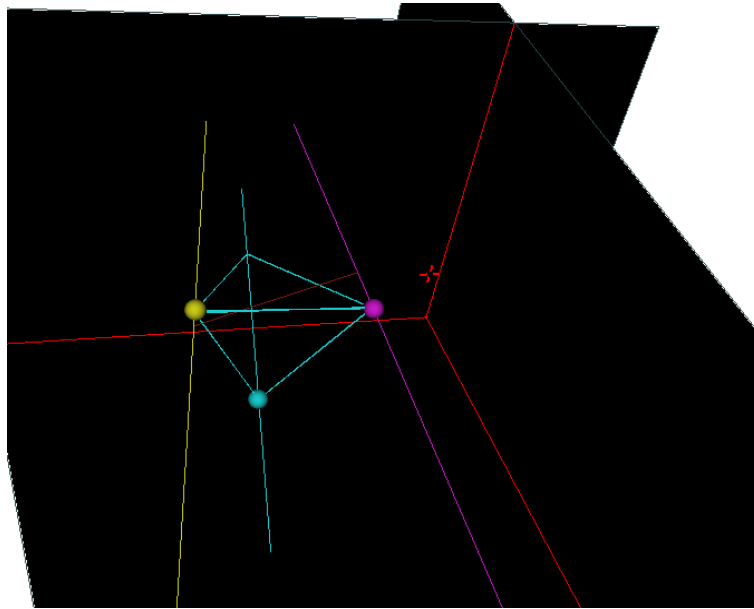


Figure 2.8: Point-to-line registration in Aatami® augmented reality environment.

## 2.4 Discussion

One advantage of the proposed method is that since needles are bright, they provide homologous features in 3D and 2D TRUS; therefore, the registration algorithm does not need to take every pixel into account. This makes the algorithm more suitable to real-time implementations where computational cost is the major issue. In other words, given the fact that registration algorithm only needs points to be segmented automatically in 2D TRUS, this registration can perform at rate of better than 20Hz provided that bright points can be segmented automatically with the same rate. However, 2D ultrasound needs to be acquired constantly during the prostatectomy procedure to track the prostate motion; therefore, if the prostate is detached from the rectal wall, then the acquisition of the ultrasound stops. This means that tracking can run until detachment of the prostate from the rectum.

In terms of physical implementation in the da Vinci robotic setting, needles need to be inserted inside the abdominal cavity through the trocar ports. In addition, before starting 3D free-hand reconstruction, the electromagnetic components of the robot need to be turned off due to the interference with the magnetic field generator.

## 2.5 Conclusion

This study developed and validated a novel 2D to 3D registration method is presented to register 2D TRUS images into 3D reconstructed TRUS so that the motion of the prostate phantom can be tracked during the planning stage of RARP. This step is employed as a component of the integration of the laparoscopic view with pre-operative MRI, in which quantified rotation and translation of the prostate is applied to the pre-operative MRI dynamically in real-time. In this manner, information regarding the distribution of the cancer within the prostate capsule can be made available to the surgeon as he/she plans resection margins. In the method described here, three needles are inserted into the prostate as reference objects to enable a transform between a peri-operatively acquired free-hand 3D TRUS image and a 2D intra-resection TRUS to be established. The efficacy of the proposed method was studied by placing the probe inside the mimicked rectum of our prostate assembly, and acquiring 2D TRUS images. These 2D slices were then registered to the peri-operatively acquired 3D TRUS images using the point-to-line registration algorithm. Since the needles are represented as being brighter than anatomical markers, they can be rapidly segmented from the image automatically. The other advantage of the proposed algorithm is that it is **not** an optimization process, and therefore issues relating to initial starting points do not affect the final results.

In order to make this method fully-automated, a Hough transform can be used to detected needles in 3D TRUS and also bright points in 2D ultrasound can be identified automatically.

# Chapter 3

## PROSTATE MOTION TRACKING USING SURFACE MARKERS

This chapter is adapted from the paper “Intra-operative prostate motion tracking using surface markers for robot-assisted laparoscopic radical prostatectomy ”, Medical Imaging 2012: Image-Guided Procedures, Robotic Interventions, and Modeling Proc. SPIE 8316, 83162N (2012)

### 3.1 Introduction

A stereoscopic tracking technique is presented in this chapter that does not require any special devices except for a few surface markers (surgical aids) pinned to the surface of the prostate to track its motion. While it may seem unusual to pierce an organ with pins to secure such a set of markers, as noted also in the previous chapters, since the prostate is to be removed immediately, there is no clinical contraindications for this approach. This method was validated in phantoms, using an optical tracking system as gold standard to assess the accuracy of the image-based stereoscopic tracking.

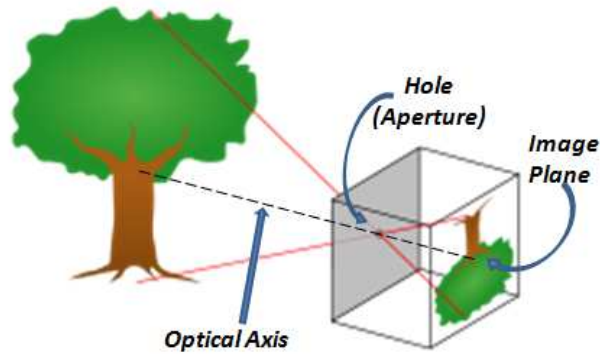


Figure 3.1: Pinhole camera model.

## 3.2 Camera Models and Calibration

### 3.2.1 Camera Model

The simplest camera model is a pinhole camera where the assumption is that light rays emanating from the scene are passing through a hole (aperture). Rays are projected on the image plane containing photosensitive cells (see Figure 3.1). In the human eye, the retina contains ganglion cells, a type of neuron to detect the visible light and differentiate between different colors. The size of the hole is assumed be less than 1/100 of its distance from the image plane. Since the final image is effectively a convolution of the ideal image and the aperture, a smaller diameter creates sharper images while the blurring increases with the increasing diameter of the aperture.

The following projection relation determines the corresponding 2D position of real objects sitting in 3D physical space.

$$x = f \frac{X}{Z}, \quad (3.1)$$

where  $f$  is the distance between the hole and the image plane (in a lens camera this is the focal distance of the lens).  $X$  is the position of the object in either horizontal or vertical direction with respect to the image plane and  $Z$  is distance of the object in the direction of viewing angle

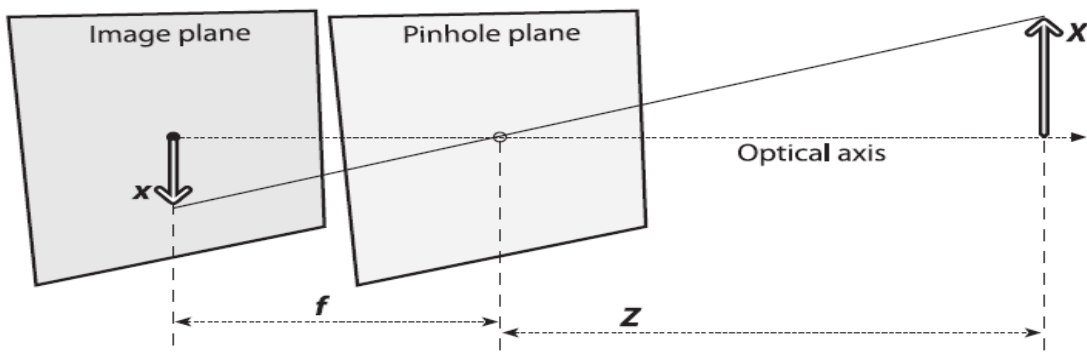


Figure 3.2: Projection relation in pinhole camera model.

(see Figure 3.2).

### 3.2.2 Distortion Model

In practice cameras are equipped with a lens to add flexibilities (such as wider aperture size), but, this comes at the expense of distorting images. In practice, rays passing closer to the margin of the lens bend more than the rays traveling through its center. This natural characteristic of the optical lens along with defects introduced during the manufacturing process leads to distortion [32], that can be modeled as a combination of radial and tangential distortion.

### 3.2.3 Radial Distortion

Radial distortion stems from the fact that parallel rays converge at the focal point of the lens. In other words, rays passing through the lens are refracted differently with respect to their distance from the optical axis of the camera. This distorts the image of an square causing its corners to look like a curved shape rather than a right-angle (see Figure 3.3).

For the simplest distortion model, the amount of distortion for each pixel of the image increases quadratically with distance [33]. The relation between the true location and distorted locations

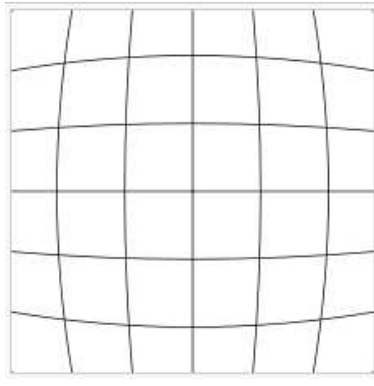


Figure 3.3: Square corners become less sharp with a curved shaped where they are far from the center of the image.

of each pixel is described by the following equation [33].

$$\begin{aligned} x_{corrected} &= x(1 + k_1r^2 + k_2r^4 + k_3r^3) \\ y_{corrected} &= y(1 + k_1r^2 + k_2r^4 + k_3r^3) \end{aligned} \quad (3.2)$$

where  $x_{corrected}$  and  $y_{corrected}$  are true locations of the pixel.  $r$  denotes the distance between center of the image and the pixel, and  $k_1$ ,  $k_2$ , and  $k_3$  are distortion coefficients. The pattern of radial distortion is illustrated in Figure 3.4, and is often is referred to as “barrel distortion”.

### 3.2.4 Tangential Distortion

Tangential distortion is caused by manufacturing defects. If the image plane is not exactly parallel to the lens, in the absence of radial distortion, squares are imaged as trapezoids. Such a distortion can be rectified using the following equation.

$$\begin{aligned} x_{corrected} &= x + [2p_1y + p_2(r^2 + 2x^2)] \\ y_{corrected} &= y + [p_1(r^2 + 2y^2) + 2p_2x], \end{aligned} \quad (3.3)$$

where  $p_1$  and  $p_2$  are tangential distortion coefficients. Figure 3.5 illustrates the tangential distortion pattern for a lens camera in pixel coordinates.

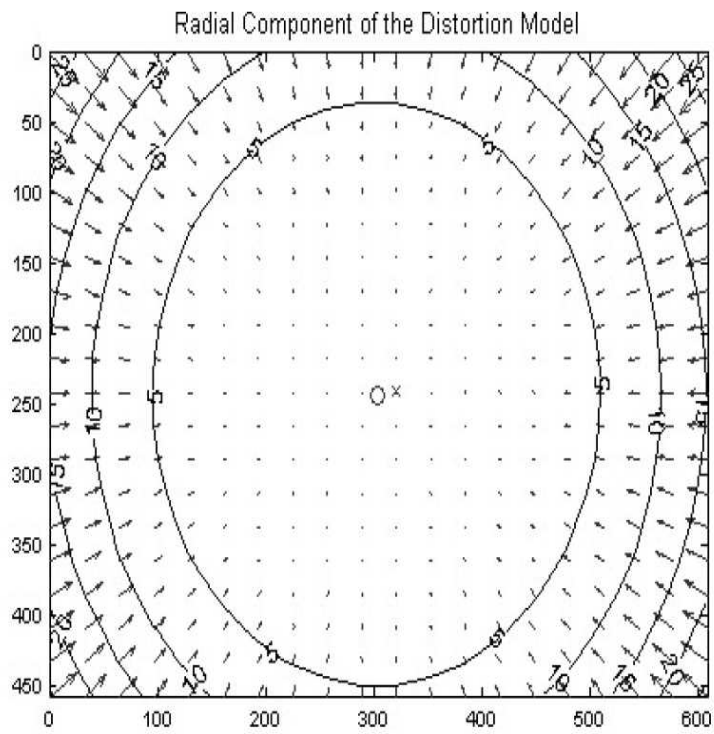


Figure 3.4: Pattern of radial distortion at different areas of a sample image. Arrows show the distance from the correct position to the distorted coordinate of the corresponding pixel.

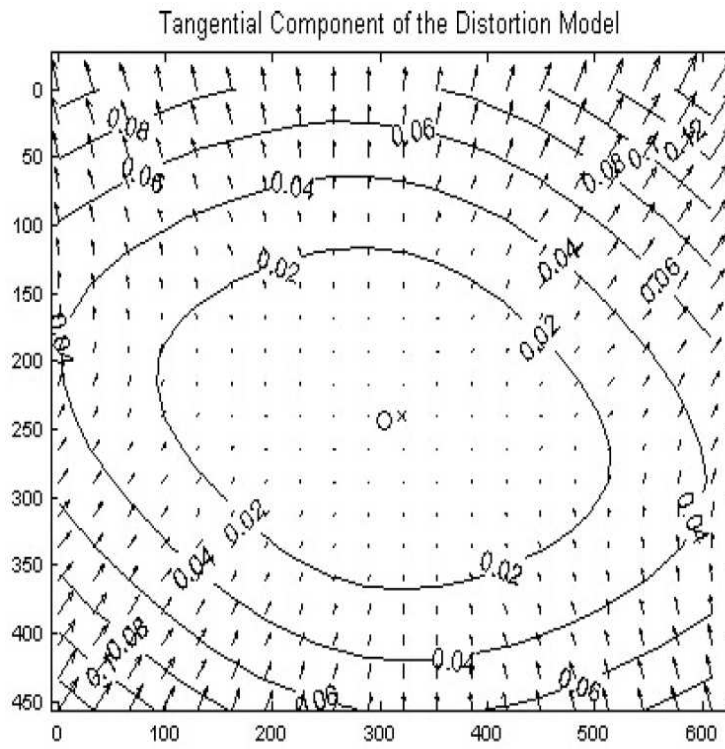


Figure 3.5: Tangential distortion pattern in pixel coordinate system for a sample image. Arrows start from the true location of the pixel to the distorted coordinate of the same pixel.



### 3.2.5 Homography

Camera calibration and triangulation are based on the homography concept whereby we can define the relationship between position of objects in 3D space and image plane of cameras. A homography relation is described by the following equation.

$$\tilde{q} = sH\tilde{Q} \quad (3.4)$$

where  $\tilde{q}$  is the 2D position of a projected 3D point  $\tilde{Q}$  on the image plane in pixel coordinates and  $s$  is scaling factor.

$H$  matrix is split into a 3D rigid transformation, bringing the world coordinate system into alignment with that of the camera coordinate system, and a camera matrix (projection part) containing intrinsic parameters of the camera matrix to perform the projection operation.

$$H = MW \quad (3.5)$$

denotes this relationship where  $W = [Rt]$  is a 4x4 matrix defining the transform from world coordinate space to the camera coordinates in homogeneous format ( $R$  is the rotation matrix and  $t$  is the translation vector), and  $M$  denotes the intrinsic parameters of the camera. The following describes the elements of camera matrix

$$M = \begin{bmatrix} f_x & 0 & c_x \\ 0 & f_y & c_y \\ 0 & 0 & 1 \end{bmatrix}, \quad (3.6)$$

where  $f_x$  and  $f_y$  are focal distance expressed in pixels in  $x$  and  $y$  directions in the image coordinate system, and  $(c_x, c_y)$  denotes the principal point where the optical axis intersects the image plane.

### 3.2.6 Endoscopic Camera Calibration

Camera calibration is the process of finding the intrinsic parameters of the camera.<sup>1</sup> Intrinsic parameters are comprised of distortion parameters and the camera matrix. There are different techniques to assess these parameters with their own costs. Two common methods have been proposed and implemented by Tsai et al. [34] and Zhang et al. [35]. While Tsai's approach provides better accuracy, it requires expensive facilities and measurements must be performed very accurately to obtain accurate calibration results. However, Zhang's method is less costly and can give good accuracy using regular facilities available in every laboratory [36].

Note that there are different measures to validate the accuracy of calibration. The most efficient measure was proposed by Weng et al. [37] who developed the Normalized Calibration Error (NCE), calculated using the following formula:

$$E_n = \frac{1}{n} \sum_{i=1}^n \left[ \frac{(\tilde{X}_{ci} - X_{ci})^2 + (\tilde{Y}_{ci} - Y_{ci})^2}{Z_{ci}^2(f_x^{-2} + f_y^{-2})/12} \right]^{0.5}, \quad (3.7)$$

where  $(\tilde{X}_{ci}, \tilde{Y}_{ci}, \tilde{Z}_{ci})$  is the triangulated position of the actual point  $(X_{ci}, Y_{ci}, Z_{ci})$  in the world coordinate system, and  $f_y$  and  $f_x$  are the focal distances of the lens in pixels in the x and y directions in vertical and horizontal directions.

### 3.2.7 Endoscope Calibration Matrix

In most augmented reality frameworks, the position of the endoscope needs to be tracked, and therefore, it is instrumented with a tracking sensor (it can be tracked using either optical or magnetic approaches). Since the relative position and orientation of the sensor and optical origin of the endoscope is not known, a calibration step is necessary to find the transform from the sensor to the camera coordinate system (centered at the optical origin of the camera). Note

---

<sup>1</sup>Note that by a lens camera, we mean a fixed focused device. The treatment of lens with variable focus is beyond the scope of this thesis.

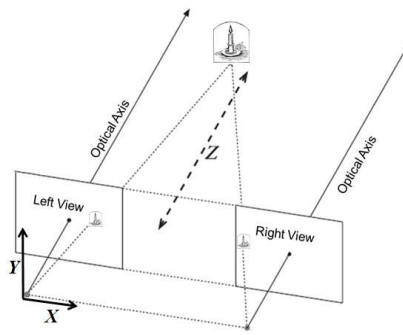


Figure 3.6: Triangulation of the points

that the calibration matrix is only a rigid map between two coordinates and it does not contain any information about intrinsic parameters of the endoscopic cameras.

### 3.2.8 Triangulation

Triangulation is the process of finding the 3D position of one point, given different views of the same point acquired from different angles (the assumption is that views are coming from different calibrated cameras with known relative location). Since each view gives a projection of the same point, at least two projections are required to find the 3D position of the same object in the world coordinates system. In other words, each projection gives us the equation of the ray emanating from the point and passing through the aperture, and therefore two rays of the corresponding object are required to find the intersection point representing the 3D location of that feature. Because a stereoscopic endoscope is equipped with two cameras, we are able find the 3D position of the corresponding features in the field of view of the endoscope.

## 3.3 Methodology

### 3.3.1 Calibration Matrix Measurement

Finding the projective relation between the 3D field of view of the laparoscope and the pixel coordinates is the first step in every augmented reality system. During this step, intrinsic and extrinsic parameters of the stereo laparoscopic cameras (Intuitive Surgical stereoscopic laparoscope from Olympus connected to a Snell & Wilcox vision cart with a Kudos Plus TBS100 synchronizer) are measured. The calibration technique used was that proposed by Zhang *et al.* [35] that images a planar checkerboard pattern from arbitrary orientations. A 6 degree-of-freedom (DOF) sensor (NDI Polaris, Waterloo ON Canada) was affixed to the stereoscopic laparoscope and then both stereoscopic laparoscopic cameras were calibrated using the OpenCV<sup>2</sup> library to assess intrinsic and extrinsic properties of each laparoscopic cameras [38, 35].<sup>3</sup> Extrinsic parameters, along with the tracking information of the dynamic reference bodies (DRB) were specifically used to measure the calibration matrix (the transform from optical origin of the left camera to the right one).

### 3.3.2 Triangulation Accuracy in Different Depths

Triangulation is employed in stereoscopic tracking to compute the 3D positions of surface markers given their 2D stereoscopic projections. Each projection provides a ray emanating from the target, and the intersection of the rays passing through the two lenses of the laparoscope determines the 3D location of the object from laparoscope point of view. However, since there is always image noise and the resolution of the digital images is limited, the accuracy of triangulation is constrained. Therefore, it is important to determine the maximum useful tracking depth [36]. To assess this depth, an optically tracked checkerboard pattern was placed

---

<sup>2</sup><http://opencv.willowgarage.com/wiki>

<sup>3</sup>Note that OpenCV uses the method of Brown *et al.* [38] to compensate for lens distortion.

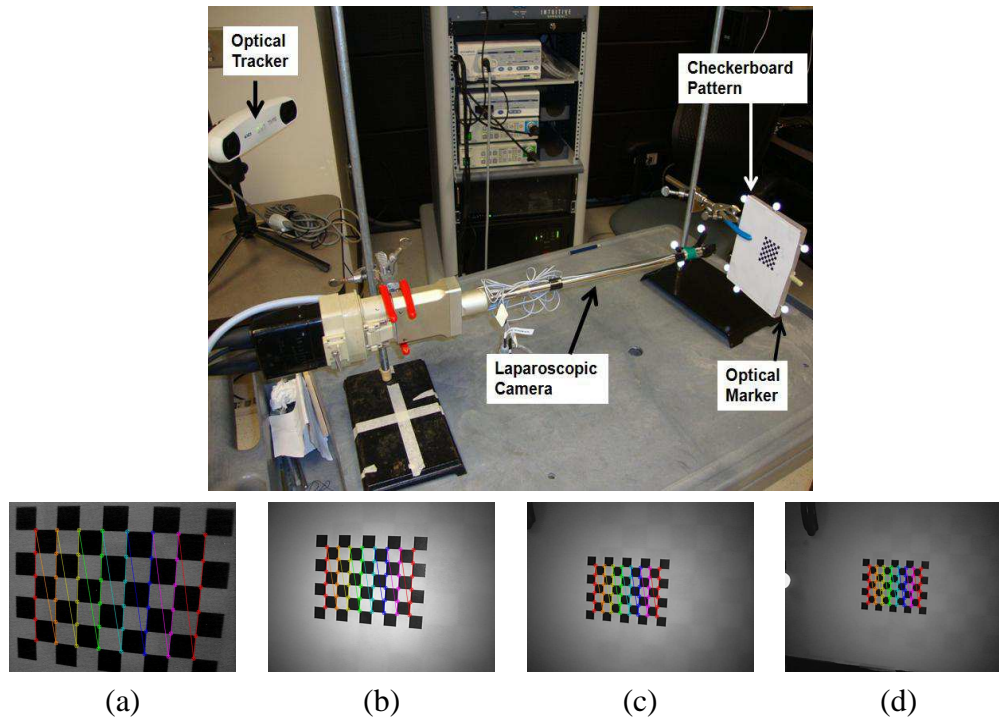


Figure 3.7: Experimental configuration for 3D triangulation of the checkerboard corners in different depths (top). Laparoscopic views of the detected checkerboard corners in depths 55, 110, 150, and 185mm from left to right (bottom).

in front of a stereoscopic laparoscope (such as is used with the da Vinci Surgical Robot) at different depths in the direction of the camera optical axis (viewing axis) (see Figure 3.7). Having two 2D stereo images, the 3D positions of the corners (used as corresponding features in the stereoscopic views) were calculated. The measured 3D positions were then compared with the true 3D locations of the corners (measured by the optical tracking system) to assess the triangulation error (see Figure 3.8).

In practice, rather than attempting to track the position and rotation of the prostate directly from anatomical surface landmarks (which are often poorly defined and suffer from specular reflection artifacts), we instead implant several easily identifiable marker pins into the prostate surface visible to the laparoscopic camera, and use those as the reference marker points.

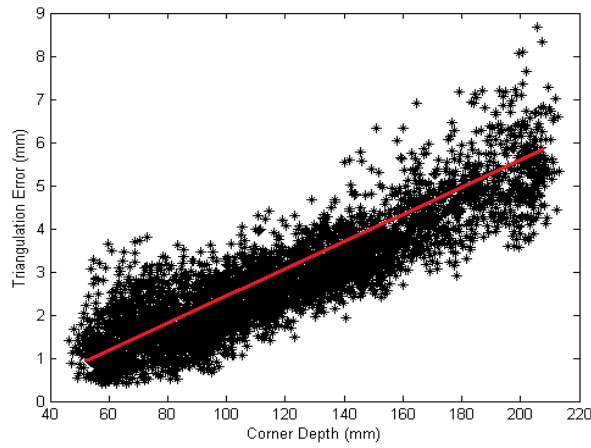


Figure 3.8: Triangulation error(mm) for corners of checkerboard pattern in different depths using stereoscopic laparoscope. Triangulation error is less than 3.5mm for corners less than 100mm far from optical origin.

### 3.3.3 Phantom Development

The prostate lies between the pubic bones, constraining rotation and translation of the prostate in a typical LRP to a maximum of approximately  $60^\circ$  and 40mm, respectively according to our surgical co-author. To simulate the prostate gland, we developed a prostate phantom using Poly-Vinyl Alcohol Cryogel (PVA-C) as a tissue-mimicking material [26]. A custom designed mold was used to shape the PVA-C to represent a realistic prostate (see Figure 3.9). Seven surface markers (wood pins, 1.8mm diameter, 7mm length) were attached to the surface along with spherical head (1.5mm in diameter, see Figure 3.10) for tracking by the stereoscopic laparoscopic cameras. Since spherical head is colour-coded it facilitates real-time feature tracking of surface markers. Also, twelve spherical Teflon<sup>®</sup> beads were implanted inside the phantom in a cross-shaped format (see Figure 3.9) for validation and a CT scan (image size  $512 \times 512 \times 173$ , spacing  $0.273 \times 0.273 \times 0.625$ mm) was acquired to represent internal structures that potentially can be provided by a pre-operative 3D DCE or T2 weighted MR image. Infra-red reflective spheres were attached to the phantom frame so that the motion of the phantom could be tracked and the resulting (gold standard) position of the embedded markers determined.

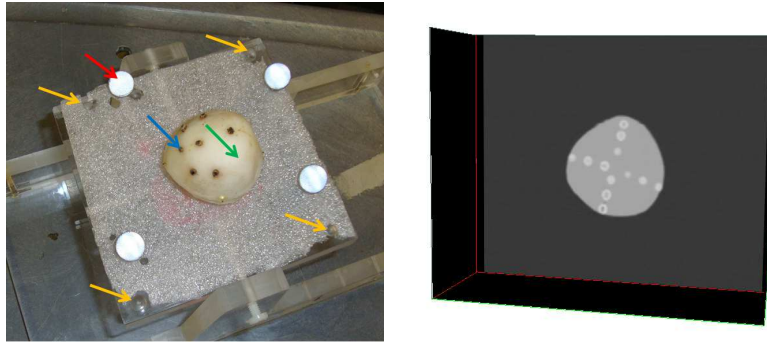


Figure 3.9: a) Prostate phantom (green arrow), divots (yellow arrows), and passive optical marker (red arrow), surface markers (blue). b) Spherical targets, Teflon<sup>®</sup> beads implanted inside the phantom as shown in CT.

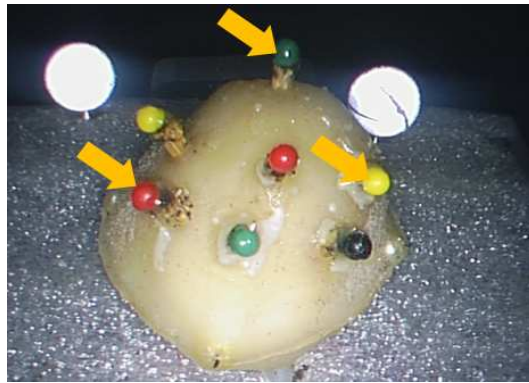


Figure 3.10: colour-coded spherical features for on-line feature detection in endoscopic video.

### 3.3.4 Surface Marker Detection

Detecting and extraction of the surface markers in real-time is a key step to perform tracking of prostate motion dynamically on-line. colour-coded sphere heads of surface markers are aimed to facilitate this process.

**Feature Extraction:** First colour-coded features<sup>4</sup> are extracted using thresholding according to their colors in HSV<sup>5</sup> colour model (thresholds for three channels are adjusted manually). The output of this step is a binary image containing seven blobs corresponding to the surface markers. One step contour detection in the binary image followed by measuring their centroids allow us to pinpoint the position of the surface marker in the pixel coordinate system.

**Feature Identification:** Finding the one-to-one correspondence between the 2D coordinate of the extracted features and that of pre-operative model is the next step. The colour of the marker is very helpful to solve this problem. Since the colour spectrum is limited, it is preferred to perform this task with fewer colors. For the purpose of this experiment, we applied three colors to identify seven features. This approach reduces the chance of overlap for colour ranges for different features and makes the entire feature tracking more robust in different lighting conditions. The two green features and two yellow features are connected by a line separately since there are only two green and two yellow features. The closest red feature to the intersection point along with the two other features at the two sides of the green line are also identified and numbered(see Figure 3.11).

### 3.3.5 Alignment Method

One efficient means of tracking the prostate motion is to track the 3D position of surface markers using triangulation and to apply the resulting transformation to the pre-operative MRI data.

---

<sup>4</sup>Practically, colors are chosen such that the colour spectra are different from prostate and surrounding tissue in the background. Green, light blue, and yellow are one possible combination.

<sup>5</sup>Hue Saturation Value.



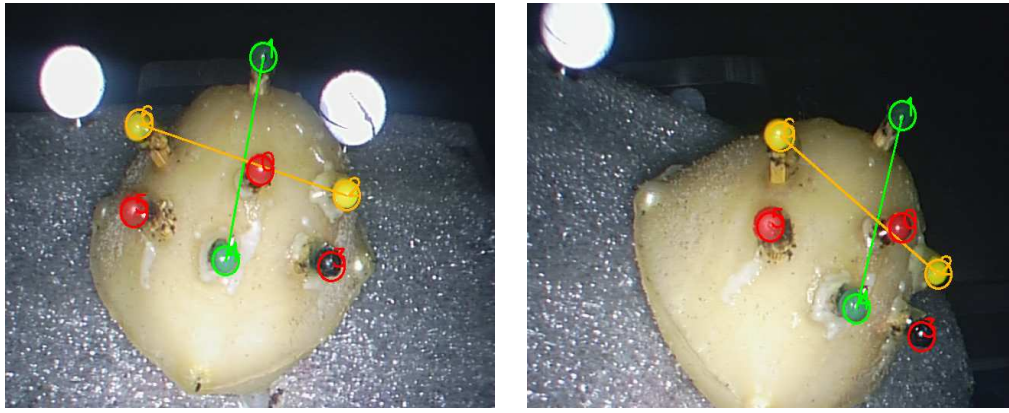


Figure 3.11: Feature extraction and identification of surface markers in endoscopic view of the prostate phantom.

The 3D positions of the surface markers are triangulated using left and right 2D laparoscopic images at the beginning of the interventional procedure, and subsequently during the procedure. A point-based tracking brings the current positions of the surface markers into alignment with the initial positions in order to compensate for the motion of the prostate with respect to its initial position. The same tracked motion can then be applied to MRI-derived pre-operative model to keep the laparoscopic view integrated with pre-operative model.

The triangulation and point based registration computation are executed at a rate of better than 20Hz, making this method suitable for tracking motion in real-time. Unlike real-time intensity based registration of ultrasound images, which ceases when the prostate is not in contact with the rectal wall (due to the air gap between the two tissues), prostate motion can be compensated during the entire procedure using stereoscopic tracking, as long as the surface markers are in the field of view of laparoscopic cameras.

In the following, we demonstrate such stereoscopic tracking of implanted surface makers to compensate prostate motion during the procedure.

To assess the 3D positions of the surface markers, first they are detected automatically in the left and right stereoscopic images acquired by the laparoscope viewing the base of the prostate phantom. Since the left and right cameras of the laparoscope are calibrated and their intrinsic

insic and extrinsic parameters are known, triangulation can determine the 3D positions of the surface markers with respect to left camera coordinate system. Having the positions of the surface markers, point-based registration determines the position of the prostate relative to the camera coordinate system. Let  ${}^{CAM}T_{PR}$  denote the corresponding transform defined during triangulation and point based registration step (see Figure 3.12). Let  ${}^{DRB1}T_{CAM}$  denote calibration matrix, the transform from the optical origin for the left lens with respect to the DRB attached to the camera calculated through the calibration process (see Figure 3.12), and  ${}^{OTS}T_{DRB1}$  is the pose of the DRB affixed to laparoscopic camera. The following equation describes the relation between the tracked position of each implanted target (interior cross-shaped spherical implanted targets denoted by  $({}^{PR}P)$ ) in the pre-operative model coordinate system (MRI-derived model coordinate system in clinical practice, but CT coordinate system for this experiment) and their homologous tracked positions in the reference frame of optical tracker measured by stereoscopic tracking:

$${}^{OTS}P = {}^{OTS}T_{DRB1} \times {}^{DRB1}T_{CAM} \times {}^{CAM}T_{PR} \times {}^{PR}P \quad (3.8)$$

where,  ${}^{OTS}P$  is the corresponding 3D position of the  ${}^{PR}P$  in the coordinate system defined by optical tracking system.

### 3.3.6 Validation

In the following we assume that the pre-operative image volume (DCE or T2 MRI in clinical practice, or the CT scan of the phantom for the the purpose of this experiment) has been accurately placed relative to the laparoscopic view either via an MR/US registration technique or via a manual image fusion technique that overlap the pre-operative image volume with the endoscopic view at the appropriate depth and scale [39, 24].

For validation purposes we employed targets simulating tumors, implanted inside the phantom.

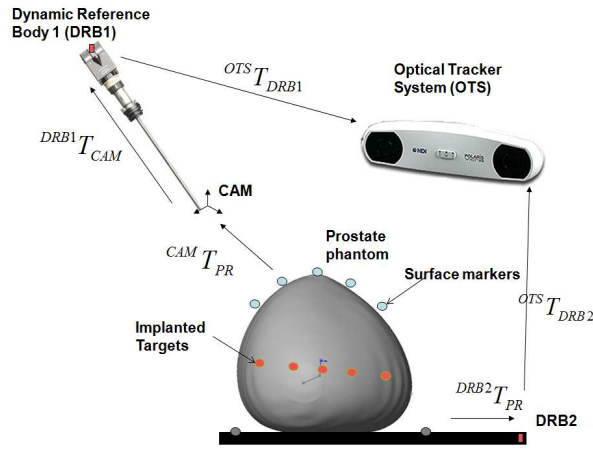


Figure 3.12: Tracking of the prostate motion using surface markers.

The ground truth locations are assessed using optical passive markers affixed to the phantom frame. The relative transform from the phantom coordinate system to optical tracking sensor (DRB2) (affixed to the phantom frame) coordinate system ( $^{DRB2}T_{PR}$ , see Figure 3.12) is determined by performing a calibration using four divots milled in the phantom frame (see Figure 3.9). This transform is applied to the known position of the implanted markers in the CT image to determine their position after applying displacements and rotations to the phantom. Also, let  $^{OTS}T_{DRB2}$  denote the position and orientation of DRB attached to phantom frame (see Figure 3.12). Having these two transforms, the true locations of the implanted markers are assessed as follows:

$$^{OTS}P^{true} = ^{OTS}T_{DRB2} \times ^{DRB2}T_{PR} \times ^{PR}P \quad (3.9)$$

where  $^{OTS}P^{true}$  is the true location of the implanted target in optical tracker coordinate system.

The typical range of translation and rotation of the prostate during a prostatectomy procedure is 40mm and 60° degrees according to our surgical colleague. Also, the laparoscopic camera observes an oblique angle with respect to the patient body. The prostate phantom was translated in different directions and rotated around three rotation axes (Anterior-Posterior (AP), Left-Right(LR), and Superior-Inferior(SI), see Figure 3.13).

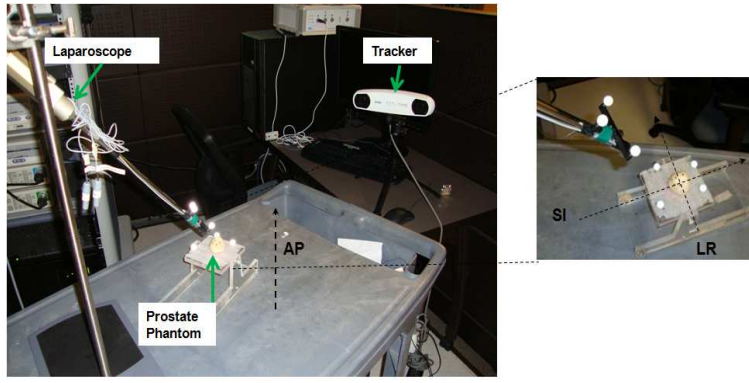


Figure 3.13: Experiment configuration.

Having inferred the tracked positions of implanted targets ( ${}^{OTS}P$ ) using the transform computed from the stereoscopic tracking, and their gold standard positions derived from the optical tracking system ( ${}^{OTS}P^{true}$ ), the target registration error (TRE) was calculated using the following equation:

$$TRE = \frac{1}{n} \sum_{i=1}^n \| {}^{OTS}P_i^{true} - {}^{OTS}P_i \| \quad (3.10)$$

where  $n$  is the number of targets and  $\|.\|$  calculates the magnitude of its argument.

### 3.4 Results

Accuracy assessment (see Figure 3.8) of triangulation in different depths shows that it can assess the 3D position with an accuracy of better than 3.5mm for corresponding features which are less than 10cm from the lenses of the laparoscope in the direction of the optical axis of camera. This depth corresponds to the typical distance of the tissue from the laparoscopic camera during RARP. At this depth, the prostate phantom was translated from -20mm to 20mm with respect to its initial position in AP, LR, and SI directions as described above. The TRE was reported for different translations represented in Table 3.1. The phantom was also rotated from  $-30^\circ$  to  $30^\circ$  around AP, LR, and SI directions (TRE reported in Table 3.2 for each rotation angle

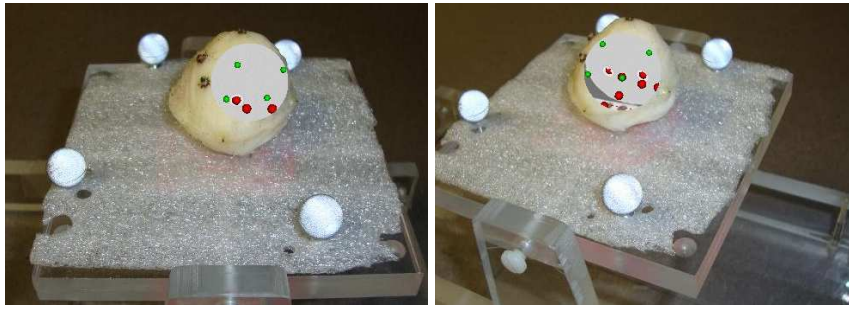


Figure 3.14: Two representative fused views of the laparoscopic cameras and 3D image volume (in ortho-plane representation) showing surface markers (green spheres) and implanted targets (red spheres).

Translation(mm)	-20	-10	0	10	20
TRE (mm) in AP	$3.24 \pm 1.21$	$2.85 \pm 1.32$	$3.38 \pm 0.93$	$2.97 \pm 1.31$	$3.34 \pm 1.11$
TRE (mm) in LR	$3.44 \pm 1.32$	$3.31 \pm 1.35$	$3.15 \pm 1.35$	$3.33 \pm 1.42$	$3.25 \pm 1.41$
TRE (mm) in SI	$3.25 \pm 1.45$	$3.32 \pm 1.13$	$3.34 \pm 1.44$	$3.15 \pm 1.36$	$3.19 \pm 1.38$

Table 3.1: TRE for different amount of translation in AP, LR, and SI directions.

for every  $15^\circ$ ). According to the aforementioned tables, the average of TRE is  $3.25 \pm 1.43$ mm which satisfies the clinically acceptable misalignment according to our surgical collaborator<sup>6</sup>.

In terms of computational complexity, image-based stereo-tracking runs at a rate of better than 20Fps. Table 3.3 reports breakdown of the timing for the different steps of this method comprised of three major steps:

1. Feature Extraction: colour based thresholding, Gaussian filtering, and contour detection proposed by Suzuki *et al.* [40].
2. Feature Identification: calculating contour centroids and identify corresponding features.
3. Triangulation (See section 3.2.8.)

---

<sup>6</sup>The clinically acceptable error has to be in the range of 3-5mm for RARP due to the fact that prostatectomy is not a targeting task and surgeons are interested in possibility of sparing neurovascular bundles.

Angle(degree)	-30	-15	0	15	30
TRE (mm) in AP	$3.12 \pm 1.32$	$3.51 \pm 1.32$	$3.15 \pm 1.23$	$3.21 \pm 1.37$	$3.18 \pm 1.21$
TRE (mm) in LR	$3.17 \pm 1.15$	$3.49 \pm 1.27$	$3.13 \pm 1.42$	$3.39 \pm 1.09$	$3.41 \pm 1.12$
TRE (mm) in SI	$3.38 \pm 1.12$	$3.57 \pm 1.34$	$3.28 \pm 1.13$	$3.31 \pm 1.20$	$2.91 \pm 1.17$

Table 3.2: TRE for different rotation angles around AP, LR, and SI directions.

Elapsed time	Feature Extraction	Feature Identification	Triangulation
secs( $10^{-3}$ )	$15.5 \pm 1.0$	$< 10^{-3}$	$0.052 \pm 0$

Table 3.3: Elapsed time for different steps of image-based stereo-tracking.

### 3.5 Conclusion

Our tracking method employs triangulation of surface markers to track prostate motion during a RARP so that the registered pre-operative images can follow the same motion to integrate with the laparoscopic view. Triangulation accuracy was assessed at different depths to determine the optimal tracking depth from the laparoscopic camera, where the tracking can perform accurately. The maximum useful tracking distance corresponded to the typical laparoscope-organ distance when performing a RARP. The prostate phantom, employed to investigate the accuracy of the tracking, had markers attached to the surface for stereoscopic tracking and also implanted targets simulating tumor for validation purposes. Motion of a prostate typically-encountered during the RARP were applied to the phantom. Three-dimensional positions of the surface markers were triangulated by their 2D positions in the left and right images of the stereoscopic laparoscope to assess rotation and translation of the prostate phantom. Measured location of implanted targets were used to assess TRE.

The main advantage of stereoscopic tracking is that it has a closed-form solution [41], and there is no issues regarding local minima. Stereoscopic tracking is also fast because it makes use of only two projection images of the targeted tissue. Besides, unlike ultrasound based tracking it can continue throughout the prostatectomy procedure even when the prostate is not connected to the rectal wall, as long as homologous markers are in the field of view of the stereoscopic laparoscope. Also, the TRUS probe is not required to remain in patient's rectum

during the prostatectomy procedure. Finally it requires minor modification (application of surface markers) to the conventional robotic clinical procedure compared to other techniques such as optical tracking proposed by Ukimura *et al.* [15] and monocular tracking by Baumhauer *et al* [19].

The future goal of this project is visualization of the enhanced view of the laparoscope in such a way that homologous features in pre-operative model and laparoscope overlap so that surgeons can see locations of the cancer foci beneath the surface of the tissue, and therefore, they can decide a better margin surrounding the prostate and make informed decisions regarding nerve sparing. Figure 3.14 illustrates representative fused views of the pre-operative image volume (CT image in this experiment) and laparoscopic views of the phantom.

# Chapter 4

## SUMMARY SUGGESTIONS AND FUTURE WORK

In this study, two prostate motion tracking techniques were investigated to compensate for prostate motion due to the interaction with the surgical tools. The first technique benefits from a 2D-to-3D ultrasound image registration technique. In spite of fast execution time of point to line registration, this method can continue as long as the prostate is connected to the rectal wall; however, stereoscopic tracking using surface markers has the chance to continue until the end of the surgery as long as surface markers are visible in the field of view of endoscope.

In comparison with methods proposed by Ukimura et al. [15], since in our method tracking and registration is performed directly through the endoscope, cumulative error does not distort the alignment. In other words, errors in tracking component and calibration (either for ultrasound probe or endoscopic camera) cannot accumulate.

In terms of suitability for real-time implementation, one advantage is that triangulation (which is the core of the computations in this method) is calculated at a rate of better than 20Hz. In addition, attachment of the surface markers allows us to find homologous features that can be segmented more easily compared to anatomical features.



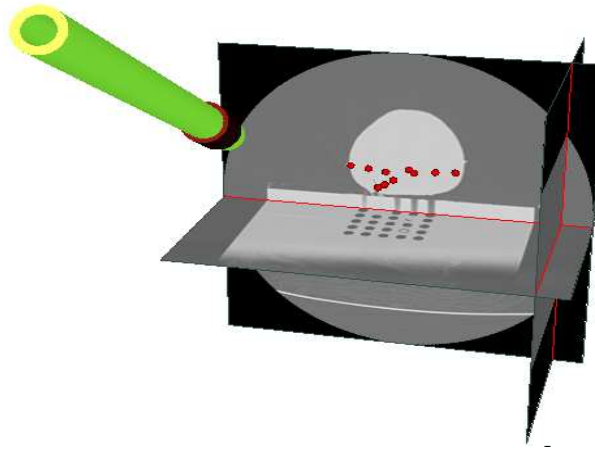


Figure 4.1: Relative position of the endoscopic camera and 3D image of the phantom in virtual reality environment.

Finally, it does not require any special device and minor modification (attachment of surface markers) is required to the regular prostatectomy procedure to track the rigid prostate motion.

Figure 4.2 illustrates representative stereo views of the proposed fusion method. Two different visualization methods were considered. The first one is superimposition of the video on the 3D image of the phantom transparently (see Figure 4.2 top). However, transparent visualization is very prone to misinterpretation in that per-operative data most of the time seem to flow over endoscopic view despite the fact that it represents the tissue beneath the tissue surface. The second visualization configuration is supposed to tackle this problem by partially occluding the preoperative image such that it is perceived underneath the video in the appropriate position in the endoscopic coordinate system (see Figure 4.2 bottom).

Figure 4.4 illustrates the same visualization configurations using a real DCE MRI of a real patient (preprocessed manually to show relative position of the tumour (blue) and neurovascular bundles (tubular lines at two sides of the prostate)) and the corresponding stereo endoscopic view of the surgical sight inside the abdominal cavity during a typical RARP. It seems qualitatively the partial occlusion of the pre-operative information provides surgeons with greater chance to perceive the fused view in the appropriate positions compared to transparent visu-

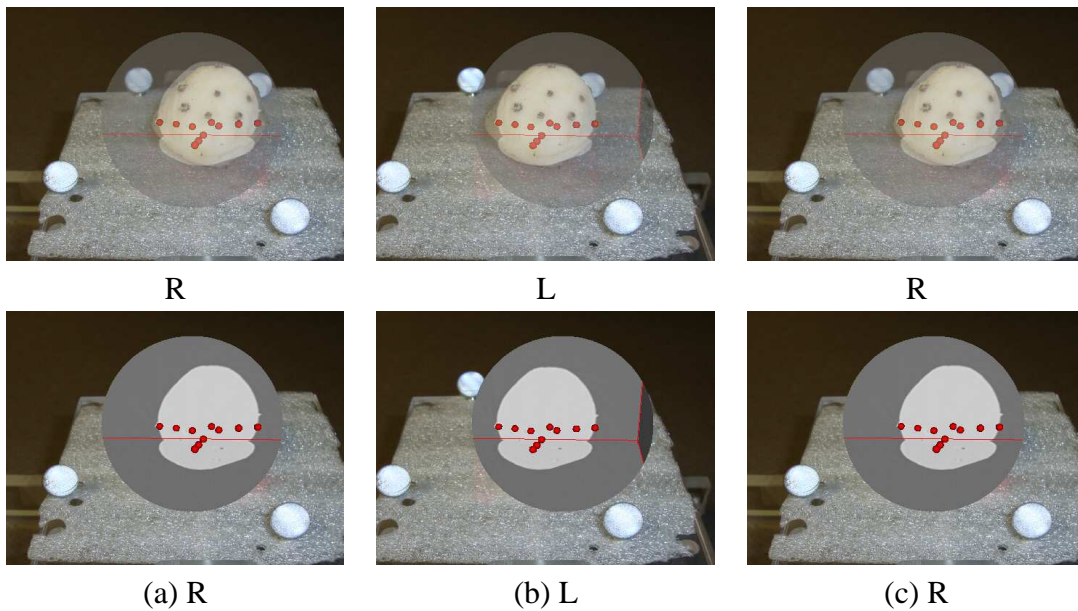


Figure 4.2: Visual assessment of transparent view of the stereo endoscope overlaid with 3D image of the phantom (Top) versus partial occlusion of the 3D image with stereo endoscopic camera (Bottom). a) and b) can be used for “cross-eye view”; b) and c) columns can be used for “wall-eye view”.

alization. However, These visualization techniques will need to be evaluated in terms of their ability to convey the appropriate depth of the intra-prostatic structures with respect to video image. It is already known that the sample fusion of two images, even if stereoscopic cues are respected in both image sets, can result in the deeper structures appearing in front of the surface as seen by the video image (Lerotic et al. [42]) so we believe that the “key=hole” approach depicted by Figure 4.2 (Top row), and Figure 4.4 (Top row) will perform more reliably than the fusion images of Figure 4.2 (Bottom row) and Figure 4.2 (Bottom row) respectively.

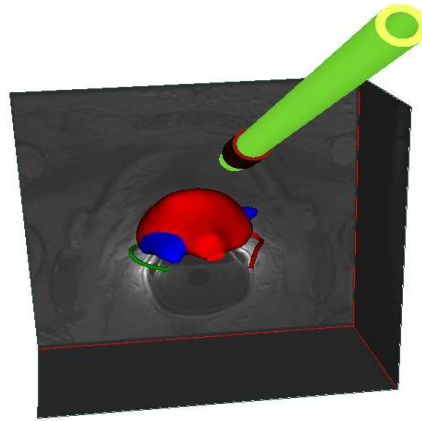


Figure 4.3: Relative position of the endoscopic camera and DCE MRI of a prostate in virtual reality environment.

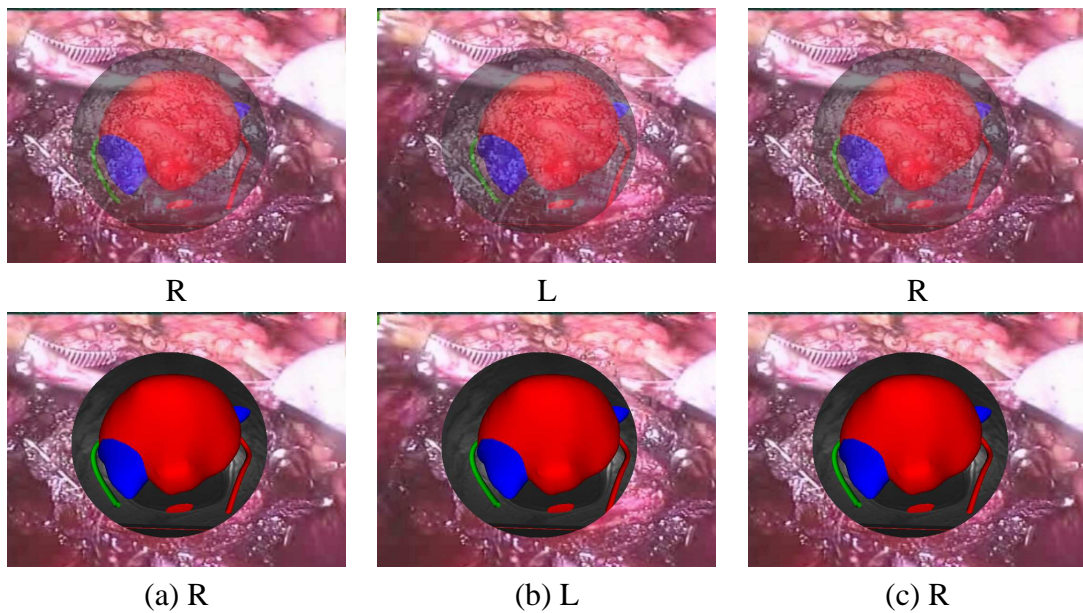


Figure 4.4: Visual assessment of transparent view of the stereo endoscope overlaid with DCE MRI (top) versus partial occlusion of DCE MRI with stereo endoscopic camera (bottom). a) and b) can be used for “cross-eye view”. b) and c) columns can be used for “wall-eye view”;



# GLOSSARY

3D-CRT	Three Dimensional Conformal Radiotherapy
CT	Computed Tomography
DCE	Dynamic Contrast Enhanced
DRB	Dynamic Reference Body
EBRT	External Beam Radiation Therapy
Gy	Gray unit
HDR	High Dose Radiation
HIFU	High Intensity Focused Ultrasound
IGI	Image Guided Intervention
IMRT	Intensity Modulated Radiation Therapy
LDR	Low Dose Radiation
LRN	Laparoscopic Radical Nephrectomy
MTS	Magnetic Tracking System
NVB	Neurovascular Bundles
ORP	Open Radical Prostatectomy
OTS	Optical Tracking System
PCa	Prostate Cancer
PLND	Pelvic Lymph Node Dissection
PSA	Prostate Specific Antigen
RARP	Robot Assisted laparoscopic Radical Prostatectomy
TRUS	TRansrectal UltraSound

# Bibliography

- [1] Newson, E., Gnreux, M., and Ascah, B., “Prostate cancer statistics,” <http://www.cancer.ca/> (2011).
- [2] <http://www.prostatecancer.ca/>, “Prostate cancer canada,” (2012).
- [3] Leissner, K. and Tisell, L., “The Weight of the Human Prostate,” *Scandinavian Journal of Urology and Nephrology* **13**(2), 137–142 (1979).
- [4] Huggins, C., Scott, W. W., and Heinen, J. H., “Chemical composition of human semen and of the secretion of the prostate and seminal vesical,” *American Journal of Physiology* **136**, 467–473 (1942).
- [5] Zhou, M. and Shah, R. B., [*Prostate Biopsy Interpretation: An Illustrated Guide*], Springer (2012).
- [6] Costello, A., Brooks, M., and Cole, O., “Anatomical studies of the neurovascular bundle and cavernosal nerves,” *British Journal of Urology International* **94**(1071) (2004).
- [7] Canada, P. C., “Prostate cancer disease states,” [www.prostatecancer.ca](http://www.prostatecancer.ca) (2012).
- [8] “Watchful waiting, the prostate cancer treatment dilemma,” <http://www.prostate-report.org/> (2012).
- [9] Oh, W. K., [*Prostate Cancer*], Mosby Elsevier (2007).
- [10] “Prostate cancer information: Cryotherapy treatment,” <http://www.prostate-cancer.com/> (2012).
- [11] Rouvire, O., Souchon, R., Salomir, R., Gelet, A., Chapelon, J.-Y., and Lyonnet, D., “Transrectal high-intensity focused ultrasound ablation of prostate cancer: Effective treatment requiring accurate imaging,” *European Journal of Radiology* **63**(3), 317–327 (2007).
- [12] Kirby, R. S., Montorsi, F., Smith, J., and Gontero, P., [*Radical Prostatectomy: From Open to Robotic*], Informa healthcare (2007).
- [13] Nelson, J., “Debate : open radical prostatectomy vs. laparoscopic vs. robotic,” **25**, 490–493 (2007).
- [14] Peters, T. M. and Cleary, K. R., [*Image-guided interventions: technology and applications*], Springer (2008).

- [15] Ukimura, O. and Gill, I. S., [*Contemporary Interventional Ultrasonography in Urology*], InTech (2011).
- [16] Ives, E. P., Burke, M. A., Edmonds, P. R., Gomella, L. G., and Halpern, E. J., “Quantitative ct perfusion of prostate cancer: Correlation with whole mount pathology,” *American Society of Clinical Oncology* **4**(2), 109–12 (2005).
- [17] Puech, P., Betrouni, N., Makni, N., Dewalle, A.-S., Villers, A., and Lemaitre, L., “Computer-assisted diagnosis of prostate cancer using DCE-MRI data: design, implementation and preliminary results,” *Int J CARS* **4**(1), 1–10 (2008).
- [18] Cohen, D., Mayer, E., Chen, D., Anstee, A., Vale, J., Yang, G., Darzi, A., and Edwards, P. E., “Augmented reality image guidance in minimally invasive prostatectomy,” *Prostate Cancer Imaging Computer-Aided Diagnosis Prognosis and Intervention* **6367/2010**, 101–110 (2010).
- [19] Baumhauer, M., Simpfendorfer, T., Miller-Stich, B. P., Teber, D., Gutt, C. N., Rassweiler, J., Meinzer, H. P., and Wolf, I., “Soft tissue navigation for laparoscopic partial nephrectomy,” *Int J CARS* **3**, 307–314 (2008).
- [20] Yip, M. C., Adebare, T. K., Rohling, R. N., Salcudean, S. E., and Ngan, C. Y., “3D ultrasound to stereoscopic camera registration through an air-tissue boundary,” *MICCAI 2010, LNCS Part II* **6362** (2010).
- [21] Silva, T. D., Fenster, A., Bax, J., Gardi, L., Romagnoli, C., Samarabandu, J., and Ward, A. D., “2D-3D rigid registration to compensate for prostate motion during 3D TRUS-guided biopsies,” *SPIE Medical Imaging, San Diego, California* **8316** (2012).
- [22] Pace, D., Gobbi, D., Wedlake, C., Gumprecht, J., Boisvert, J., Tokuda, J., Hata, N., and Peters, T., “An open-source real-time ultrasound reconstruction system for four-dimensional imaging of moving organs,” *Medical Image Computing and Computer Assisted Intervention (MICCAI)* **1682**, 123–131 (September 2009).
- [23] Karnik, V., Fenster, A., Bax, J., Gardi, L., Gyacskov, I., Montreuil, J., Romagnoli, C., and Ward, A., “Evaluation of inter-session 3D-TRUS to 3D-TRUS image registration for repeat prostate biopsies,” *Medical Image Computing and Computer Assisted Intervention (MICCAI), LNCS* **6362**, 17–25 (2010).
- [24] Narayanan, R., Kurhanewicz, J., Shinohara, K., Crawford, E., Simoneau, A., and Suri, J., “MRI-Ultrasound registration for targeted prostate biopsy,” *Biomedical Imaging: From Nano to Macro, 2009. ISBI '09. IEEE International Symposium on*, 991–994 (July 2009).
- [25] Karnik, V., Fenster, A., Bax, J., Gardi, L., Gyacskov, I., Montreuil, J., and Romagnoli, C., “Assessment of image registration accuracy in three-dimensional transrectal ultrasound guided prostate biopsy,” *Medical Physics* **37**(2), 802–13 (2010).
- [26] Surry, K. J. M., Austin, H. J. B., Fenster, A., and Peters, T. M., “Poly(vinyl alcohol) cryogel phantoms for use in Ultrasound and MR imaging,” *Phys In Med & Biol* **49**(24), 5529–46 (2004).

- [27] Soto, E., Karnik, V., Gyacskov, I., Gardi, L., Poepping, T. L., Campbell, G. J., Fenster, A., and McKenzie, C. A., "Assessment of registration accuracy between magnetic resonance imaging and three dimensional trans-rectal ultrasound imaging of prostate cancer," *Technical Report: International Society for Magnetic Resonance in Medicine* **8**, 2243–48 (2009).
- [28] Schonemann, P. H., "A generalized solution of the orthogonal procrustes problem," *Psychometrika* **31**(1), 1–10 (1966).
- [29] Farrell, J., Stuelpnagel, J., Wessner, R., Velman, J., and Brock, J., "Solution 65-1: A least squares estimate of satellite attitude," *SIAM Rev.* **8** (1966).
- [30] Cheung, C. L., Wedlake, C., Moore, J., Pautler, S. E., Ahmad, A., and Peters, T. M., "Fusion of stereoscopic video and laparoscopic ultrasound for minimally invasive partial nephrectomy," *Proceedings Medical Imaging* **7261** (2009).
- [31] Pace, D., Gobbi, D., Wedlake, C., Gumprecht, J., Boisvert, J., Tokuda, J., Hata, N., and Peters, T., "An open-source real-time ultrasound reconstruction system for four-dimensional imaging of moving organs," *Medical Image Computing and Computer Assisted Intervention (MICCAI)* (September 2009).
- [32] Bradski, G. and Kaehler, A., [*Learning OpenCV Computer Vision with the OpenCV Library*], O'Reilly Media (2008).
- [33] Brown, D., "Decentering distortion of lenses," *Photogrammetric Engineering* **7**, 444–462 (1966).
- [34] Tsai, R., "A versatile camera calibration technique for high accuracy 3D machine vision metrology using off-the-shelf tv cameras and lenses," *IEEE J. Robotics and Automation* **3**(4), 323–344 (1987).
- [35] Fix, M. and Zhang, Z., "Flexible camera calibration by viewing a plane from unknown orientations. in: Proceedings of the 7th international conference on computer vision," *Urology* **61**, 612–616 (Mar. 2003).
- [36] Sun, W. and Cooperstock, J., "Requirements for camera calibration: Must accuracy come with a high price?," *Application of Computer Vision, 2005. WACV/MOTIONS '05 Volume 1. Seventh IEEE Workshops on* , 356–361 (2005).
- [37] Weng, J., Cohen, P., and Herniou, M., "Camera calibration with distortion models and accuracy evaluation," *IEEE Trans. Patt. Anal. and Machine Intell.* **14**(10), 965–980 (1992).
- [38] Brown, D., "Close-range camera calibration," *Photogrammetric Engineering* **37** (1971).
- [39] Esteghamatian, M., Pautler, S. E., McKenzie, C. A., and Peters, T. M., "A 2D to 3D ultrasound image registration algorithm for robotically assisted laparoscopic radical prostatectomy," *SPIE Medical Imaging 2011 (7962-70)* (2011).
- [40] Suzuki, S. and Abe, K., "Topological structural analysis of digital binary images by border following.," *Computer Vision, Graphics and Image Processing* **30**, 32–46 (1985).



- [41] Hartley, R. I. and Sturm, P., “Triangulation,” *Computer Vision and Image Understanding* **68**, 146–157 (1997).
- [42] Lerotic, M., Chung, A. J., Mylonas, G. P., and Yang, G.-Z., “Pq-space based non-photorealistic rendering for augmented reality.,” in [*MICCAI (2)’07*], 102–109 (2007).

# Appendix A

## Copyright Use Permission

Figures 1.15 - 1.24	<p>Courtesy Dr. Robert a Leung. Used with permission.</p> <p><i>From: Robert A. Leung</i> <i>Sent: May-22-12 8:41 AM</i> <i>To: Terry Peters</i> <i>Subject: message</i></p> <p><i>Prof. Peters:</i></p> <p><i>I received your message. Please feel free to use screen captures and video clips related to our materials. I'd request that the images be properly cited.</i></p> <p><i>Taking a look at your lab website, there are certainly a lot of opportunities for us to collaborate. We are currently working on a several imaging modalities for prostate cancer. Perhaps we can have a phone conference in the near future to discuss.</i></p> <p><i>Robert</i></p>
Figure 3.4 and Figure 3.5	Courtesy <b>Learning OpenCV Computer Vision with the OpenCV Library</b> By Gary Bradski, Adrian Kaehler, O'Reilly Media, September 2008
Figure 1.12	Courtesy WebMD ( <a href="http://www.webmd.com/">http://www.webmd.com/</a> ). Used with permission.
Figure 1.13	Courtesy <a href="http://www.psc.edu/">http://www.psc.edu/</a> . Used with permission.

Figure 1.1	<p>Courtesy <a href="http://www.healthadviceonline.biz/">http://www.healthadviceonline.biz/</a>. Used with permission.</p> <p><i>from: Cherie Ang</i> <i>to: Mehdi Esteghamatian</i> <i>date: Sat, May 26, 2012 at 10:57 PM</i> <i>subject: Re: Copyright</i></p> <p><i>Hi Medhdi,</i></p> <p><i>Since you have acknowledged my website, I have no concerns about the copyright.</i></p> <p><i>Thanks for visiting my blog.</i></p> <p><i>Best Regards,</i> <i>Cherie</i></p>
------------	---

# Curriculum Vitae

<b>Name:</b>	Mehdi Esteghamatian
<b>Year of Birth</b>	1982
<b>Post-Secondary Education and Degrees:</b>	Computer Engineering Shiraz University 2005 - 2008 M.Sc.
<b>Honours and Awards:</b>	NSERC CREATE Program in Computer-Assisted Medical Intervention Scholarship (2009-2011)
<b>Teacher Assistantship</b>	<b>Digital Image Processing</b> - Lecturer Dr. H. Ladak <b>Programming Fundamentals for Engineers</b> - Lecturer Dr. Q. Rahman <b>Data Storage and Retrieval</b> - Lecturer Dr. G. Dastgheibifard

## Conference Proceedings:

M. Esteghamatian, E. Chen, K. Sarkar, S.E. Pautler, and T.M. Peters, "Prostate motion tracking using surface markers for laparoscopic radical prostatectomy: a phantom study", Proc. SPIE Medical Imaging 2012: Image-Guided Procedures, Robotic Interventions, and Modeling, no. 8316-96, 2012, San Diego, USA.

M. Esteghamatian, S.E. Pautler, C.A. McKenzie, and T.M. Peters, "2D to 3D ultrasound image registration algorithm for robotically assisted laparoscopic radical prostatectomy", Proc. SPIE Medical Imaging 2011: Image Processing, 7962, 79621Z, 2011, Florida, USA.

M. Esteghamatian, A. Kazemi, Z. Azimifar, P. Radau and G. Wright, "Real-Time MR Cardiac Image Registration During Respiration: A Neural Network Approach", International Conference On Signal Processing IEEE, 2008, Beijing, China.

M. Esteghamatian, Z. Azimifar, P. Radau and G. Wright, "Real-Time 2D-3D MR Cardiac Image Registration During Respiration Using Extended Kalman Filter Predictors", International

Confer- ence On Signal Processing IEEE, 2008, Beijing, China.

M. Esteghamatian, Z. Azimifar, P. Radau and G. Wright, “A Framework Toward 2D-3D MR Cardiac Image Registration During Respiration for MRI-guided Procedures”, 16th Iranian Conference on Electrical Engineering, 2008, Tehran, Iran.

### **Peer Reviewed Journals**

M. Esteghamatian, Z. Azimifar, P. Radau and G. Wright, “Real Time Cardiac Image Registration During Respiration: A Time Series Prediction Approach”, Journal of Real-Time Image Processing, pp 1-13, April 2011